CHALMERS
UNIVERSITY OF TECHNOLOGY

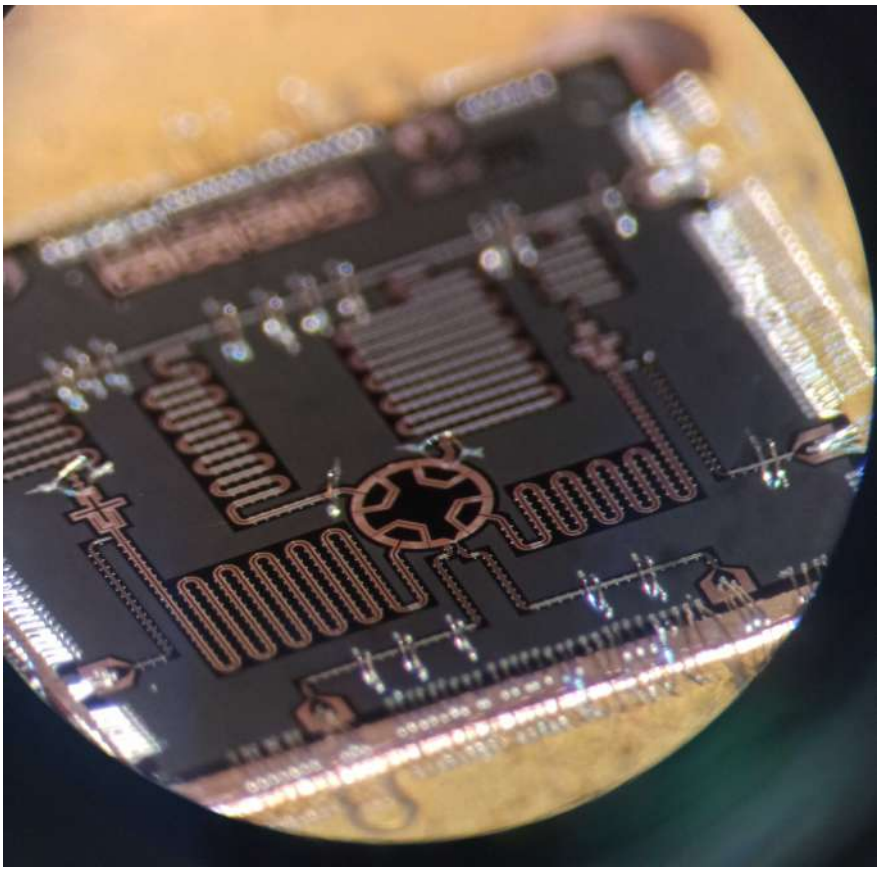

Extensible tunable coupling between bosonic modes in superconducting circuits

Master's thesis in Erasmus Mundus Master in Nanoscience and Nanotechnology

VERONIKA BELIAEVA

DEPARTMENT OF SOME SUBJECT OR TECHNOLOGY
CHALMERS UNIVERSITY OF TECHNOLOGY
Gothenburg, Sweden 2023
www.chalmers.se

Master's thesis 2023

Extensible tunable coupling between bosonic modes in superconducting circuits

VERONIKA BELIAEVA

CHALMERS
UNIVERSITY OF TECHNOLOGY

Department of Microtechnology and Nanoscience
Quantum Technology Laboratory (QT)
202Q-lab
Chalmers University of Technology
Gothenburg, Sweden 2023

Extensible tunable coupling between bosonic modes in superconducting circuits

Supervisor: Dr. Axel Eriksson, Quantum Technology Laboratory (QT)
Examiner: Asst. Prof. Simone Gasparinetti, Quantum Technology Laboratory (QT)
Co-promoter: Bart Sorée, KU Leuven

Master's Thesis 2023
Department of Microtechnology and Nanoscience
Quantum Technology Laboratory (QT)
202Q-lab
Chalmers University of Technology
SE-412 96 Gothenburg
Telephone +46 31 772 1000

Cover: An optical microscope image of the designed chip after being wire bonded to the planar circuit board.

Typeset in LaTeX
Printed by Chalmers Reproservice
Gothenburg, Sweden 2023

Extensible tunable coupling between bosonic modes in superconducting circuits
VERONIKA BELIAEVA
Department Microtechnology and Nanoscience (MC2)
Chalmers University of Technology

Abstract

Bosonic quantum computing utilizes the high dimensionality of harmonic oscillators to encode and manipulate quantum information. Superconducting planar circuits offer a promising platform for creating quantum computing chips, enabling universal control over individual bosonic modes via ancillary superconducting qubits. To achieve universal control in a multi-mode system, the extension of control through two-mode gates is sufficient. An example of a two-mode gate is a beamsplitter, which is a natural and easily achievable element in superconducting circuits. The physical realization of this gate involves connecting microwave resonators through a tunable coupler. In this project, we design a planar superconducting platform hosting four individual modes, each coupled to a Superconducting Nonlinear Asymmetric Inductive eLement (SNAIL)-based single coupler, leading to a fully connected system. Fine-tuning the SNAIL coupler's potential allows in-situ cancellation of the unwanted nonlinear Kerr interactions, making it a suitable connectivity element. After the fabrication of the designed chip, we experimentally characterize its parameters and demonstrate beamsplitting through parametric flux modulation. To visualize and validate the experimental results, we employ Wigner tomography on one of the cavities' quantum state. The demonstrated SNAIL-based intercavity beamsplitter interaction could open new pathways for two-mode gate mechanisms by simultaneously beamsplitting pairs of modes in a highly interconnected system.

Acknowledgements

I would like to express my sincere gratitude to my supervisor, Axel Eriksson, for his guidance and insightful leadership during the course of this project.

I am deeply thankful to Mikael Kervinen for fabricating the device for this study. I am grateful to the rest of my colleagues from 202Q-lab for their generous assistance with the setup as well as for their constant help and advice.

I would like to acknowledge my examiner, Prof. Simone Gasparinetti, for giving me the opportunity to participate in this project within the 202Q-lab. His insights and evaluations have been invaluable, providing me with a clear understanding of the level of awareness I should aim for in my work.

My appreciation also goes out to my friends and colleagues who gave me both a supportive network and moments of friendly competition during our ping pong sessions.

Veronika Beliaeva, Gothenburg, August 2023

Contents

1
Introduction

Over the past few decades, quantum computing has introduced multiple promising insights into computational problems and algorithms that surpass classical computers. [1, 2, 3] A variety of approaches for quantum computing realization have been demonstrated. Today, superconducting circuits remain one of the most advanced and capable platforms for physical implementation of a quantum computer. [4] Introducing the opportunity of macroscopic lithographically defined configuration allows to construct adjustable effective two-level systems and insert them into scalable architectures. [5]

An alternative approach for processing quantum information is encoding a qubit in continuous-variable (CV) paradigm implementing bosonic modes such as harmonic oscillators. [6] This approach proposes several advantages in comparison to discrete quantum computing, because it makes possible significant scaling [7] and fault-tolerant computation codes [8, 9], which allow hardware-efficient error-correction. [10]

There are two distinctive architectures of superconducting bosonic quantum systems: planar and three-dimensional (3D). 3D-based resonator structures are designed as a vacuum chamber with resonator structure inside (for instance, stub geometry resonator schematically depicted in Fig. 1.1a). Since the electro-magnetic field lives in vacuum, with 3D circuits it is possible to achieve significant coherence times [11] and these circuits are therefore often referred to as quantum memory [12]. However, it is challenging to produce high quality 3D cavities and further scale them to connect a larger number of logical qubits. An example of a planar resonator constructed from a coplanar waveguide is shown in Fig. 1.1b. Such planar architectures are patterned by means of lithography methods, which makes them easy-fabricating and compact. Additionally, planar structures enable improved control over the coupling strengths as compared to 3D arrangements, where the chips are manually inserted.[13]

In superconducting binary circuits, a two-level system is established by implementing a Josephson junction as a nonlinear inductance in LC-circuit (see, e.g., [16] for detailed treatment of this phenomena). In the continuous-variable paradigm, the basis states $|0\rangle$ and $|1\rangle$ of a bosonic qubit are encoded as superpositions of the Fock states of the oscillator. However, nonlinearity is crucial for universal control to provide the ability to manipulate the quantum information. In the context of superconducting planar circuits, a viable method to achieve universal multi-mode quantum computing involves establishing a universal control over a single bosonic

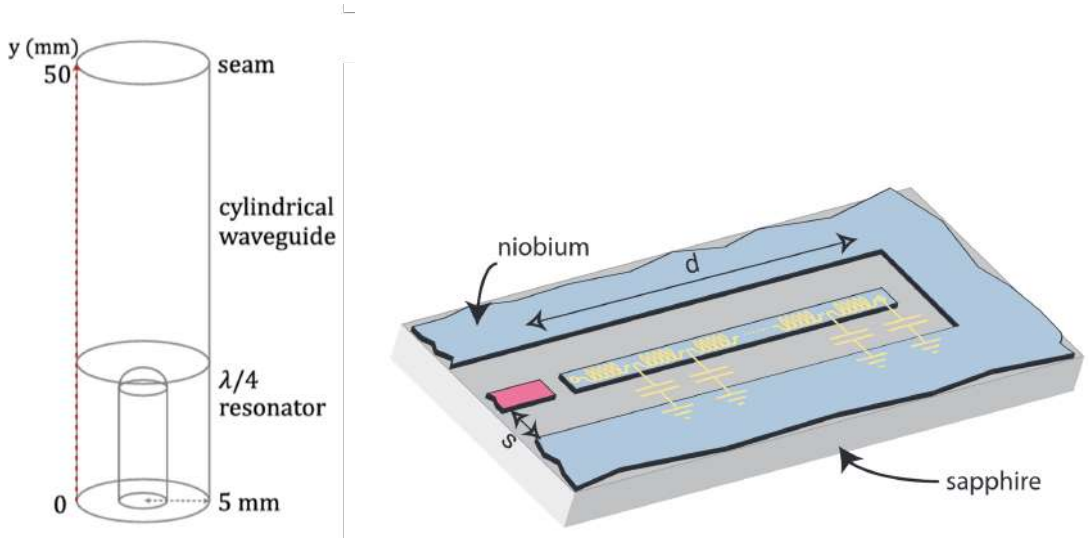

(a) **(b)**

Figure 1.1: Examples of resonator structures for a) [14] 3D architectures b) [15] planar architectures. Here, d is resonator length, s – gap separation from the ground plane. Blue color represents metallic material, grey – wafer substrate, red – electromagnetic environment.

mode, e.g. via dispersive coupling to a transmon qubit [17]. Subsequently, the multi-mode control is accomplished through intermode coupling. Connectivity between bosonic modes is thus a necessary building block for multi-mode universal control. As long as inter-mode communication is established in a manner that enables any mode to interact with any other mode, the connectivity can be considered as sufficient. However, implementing connectivity of all modes to one another enables rapid and efficient quantum computing perspectives.

Examples of nonlinear intermode connectivity elements introduced into superconducting circuits vary significantly. For instance, propagation of microwave fields and its interaction with each other was observed for cavities coupled via a transmon [20], or a SQUID [21, 26]. SQUIDs were also used for investigation on quantum state storage [22], entanglement [23], on-demand transition [24] and release [25]. A transmon was used to realize interference between two microwave modes in a four-wave parametric process [27] and a Josephson junction was used to perform the process of quantum states confinement on a quantum manifold spanned by two coherent states. [28]

Once universal control over a single mode is achieved, establishing connectivity among multiple modes becomes crucial for multi-mode quantum computing. However, if non-Gaussian states can be accessed through qubit-resonator entangling gates, a Gaussian interaction for a two-mode gate is sufficient for universal multi-mode control. Among the variety of possible two-mode entangling Gaussian gates, beamsplitter gate is one of the most natural and easy-achievable gates in superconducting circuits. [39, 34]

To attain fast and efficient beamsplitting via coupling and further parametric modulation of the circuit, it is necessary to satisfy several requirements for the coupler

- It allows to achieve a high-fidelity process.
- It implements a high on/off interaction ratio, which is necessary for precise gate performance control. When one performs operations which involve several bosonic states, it is crucial to distinguish which modes are interacting.
- It reduces the effect of unwanted nonlinear effects. Coupling to nonlinear circuits is essential to attain a universal multi-mode control. However, nonlinearity is also a source of unwanted high-order effects. Particularly, quartic-order Kerr interactions lead to state distortion and decoherence. [12] A good coupler allows by its design to reduce the effect of these unwanted parasitic terms.

Recently a dipole device based on an array of Josephson junctions was introduced, which was called Superconducting Nonlinear Asymmetric Inductive eLement (SNAIL). [29] The coefficients in Taylor expansion of its potential energy depend on the external flux. It can be shown that for the potential of this particular element it is possible to achieve the third-order nonlinear potential putting the fourth-order Kerr term to zero, i.e. achieve cubic nonlinearity without the Kerr one. This unique feature became a source of inspiration for various investigations on parametric bosonic interactions [30, 31, 32, 39].

In this work we design, fabricate, demonstrate the performance of a planar platform for multiple bosonic modes with a SNAIL-based coupling and efficiently implement a beamsplitting gate between microwave cavities.

2
Theory

The focus of the thesis is on the design and characterization of the chip intended for interaction between bosonic modes. This chapter introduces the fundamental concepts for continuous variable quantum computing, discusses the theoretical aspects of a SNAIL element, provides a topological definition of the future circuit, and describes two distinct approaches for beamsplitting.

2.1 Continuous variables

Continuous variable quantum computing (CV QC), in comparison to discrete QC, enables the performance of operations on observables (amplitude and phase quadratures) with a continuous spectrum

$$\hat{p} = \frac{\hat{a} + \hat{a}^\dagger}{\sqrt{2}} \tag{2.1}$$

and

$$\hat{q} = \hat{a} - \hat{a}^\dagger i\sqrt{2}, \tag{2.2}$$

where $\hat{a}$ is the annihilation operator of a particular bosonic system. These operators obey the commutation relation

$$[\hat{p}, \hat{q}] = i, \tag{2.3}$$

thus satisfying the Heisenberg uncertainty principle. The Hilbert space associated with this bosonic system is infinite-dimensional, the energy eigenvalues of this space are corresponding to the number operator $\hat{n} = \hat{a}^\dagger\hat{a}$. The eigenvectors of the number operator $\hat{n}\,|n\rangle = n\,|n\rangle$, where n represents the number of photons in the system, in turn form the basis of the bosonic system, which is called Fock basis.

One can define the eigenstate of the annihilation operator $\hat{a}\,|\alpha\rangle = \alpha\,|\alpha\rangle$ as a coherent state – the definition refers to the fact that this state keeps the largest resemblance to a classical state with respect to its quasi-probability distribution picture in contrast to other quantum states. One can show [42] that

$$|\alpha\rangle = e^{\frac{-|\alpha^2|}{2}} \sum_{n=0}^{\infty} \frac{\alpha^n}{\sqrt{n!}}\,|n\rangle\,. \tag{2.4}$$

Calculating the average number of photons in a coherent state provides with the following distribution

$$|\langle\alpha|\,\hat{n}\,|\alpha\rangle| = e^{-|\alpha|^2}\frac{|\alpha|^{2n}}{n!}, \tag{2.5}$$

in which one can recognize Poisson distribution.

The fact that electromagnetic field quadratures do not commute (eq. 2.3) implies that it is impossible to define a position of the system in the (p, q) phase space with defined amplitude and phase simultaneously. However, one can define a quasiprobability distribution to visualize and characterize continuous variable states. Such a quasiprobability function that is one of the most commonly used for CV QC is Wigner function, which can be defined as follows

$$W(x,y) = \frac{1}{\pi}\int du e^{2iyu} \langle x + \frac{u}{2}| \hat{\rho} |x - \frac{u}{2}\rangle , \tag{2.6}$$

where $\alpha = x + iy$, $\hat{\rho}$ is the density matrix of the system. A notable attribute of the Wigner function is its direct measurability in circuit quantum electrodynamics through the process of Wigner tomography. To perform this tomography, a system of a resonator cavity and dispersively coupled qubit is required. It can be shown [42] that

$$W(x,y) = \frac{1}{\pi}\int du e^{2iyu} \langle x + \frac{u}{2}| \hat{\rho} |x - \frac{u}{2}\rangle = \frac{2}{\pi} \mathrm{Tr}\left[\hat{D}(-\alpha)\hat{\rho}\hat{D}(\alpha)\mathcal{P}\right], \tag{2.7}$$

where $\hat{D}(\alpha)$ is displacement operator, $\hat{\mathcal{P}}$ is the parity operator. Equality 2.7 means that to measure Wigner function, i.e. to perform Wigner tomography, one needs to displace a state $\hat{\rho}$ in phase space by α and subsequently measure the expectation value of the parity operator with that state (due to the density matrix property which states $\langle\mathcal{P}\rangle = \mathrm{Tr}\left[\hat{\rho}\mathcal{P}\right]$). Parity can then be mapped to the dispersively coupled qubit state, as it is discussed in experimental chapter, sec. Wigner tomography protocol. States with a positive-definite Wigner distribution function in phase space that exhibits a Gaussian-like shape are referred to as Gaussian states.

2.2 Universal gate set

According to the pioneer investigation on universality for CV approach [6], a set of CV quantum operations is universal if one can simulate arbitrarily closely the action of any Hamiltonian by a finite number of the operator applications. One of possible universal set for single-mode Gaussian operations is known and contains, for instance, quadrature displacement

$$D_{1,q}(s) = e^{is\hat{q}}, \tag{2.8}$$

shear (quadratic in the quadratures)

$$D_{2,q}(s) = e^{\frac{is\hat{q}^2}{2}} \tag{2.9}$$

and quadrature rotation (also quadratic in the quadratures)

$$R(\theta) = e^{\frac{i\theta(\hat{q}^2+\hat{p}^2)}{2}}. \tag{2.10}$$

However, algorithms that rely solely on Gaussian unitaries manipulating Gaussian states can be simulated efficiently on a classical computer. [40] On the contrary, in superconducting CV circuits framework, nonclassicality of the quantum states is achieved via dispersive coupling between linear harmonic oscillators and a qubit with subsequent implementation of cavity-qubit entangling gate, for instance, selective number-dependent arbitrary phase (SNAP) [43] or echoed conditional displacement (EDC) [41] gates. Hence, by a precise control in the system universality over one-mode non-Gaussian state can be achieved. Note, that dispersive regime is essential for the ability to resolve Fock level peaks corresponding to the cavity state in the qubit spectrum. This enables mapping of the cavity parity to the qubit.

With universal control over a single mode attained, connectivity among multiple modes is essential for multi-mode quantum computing. Since non-Gaussian states are accessible with qubit-resonator entangling gates, for two-mode gate it is enough to perform Gaussian, i.e. quadratic on quadratures, interaction. In this thesis, the focus is on the beamsplitting operation, which can be represented in terms of quadratures as

$$B_{12} = e^{i\frac{\pi}{2}(\hat{p}_1\hat{q}_2 - \hat{p}_2\hat{q}_1)}, \tag{2.11}$$

according to [38]. Here, $\hat{p}_1, \hat{q}_1$ are quadrature operators of one mode, $\hat{p}_2, \hat{q}_2$ are of another. (2.11) in combination with controllable non-Gaussian single-mode quantum states gives the universality for multi-mode quantum computing.

2.3 Coupling for beamsplitter gate implementation

A coupling element that allows to implement mode interaction in a controllable way is needed. In this section, a proposal for the structure of this element is presented, along with the reasoning behind this choice.

2.3.1 Beamsplitter Hamiltonian

Consider two coupled bosonic modes with annihilation operators $\hat{a}$ and $\hat{b}$, which pass through a beam splitter (Fig. 2.1a).
Hamiltonian of beamsplitting interaction, corresponding to the gate 2.11 in the interaction picture

$$\frac{\hat{H}_{bs}}{\hbar} = g_{bs}(t)\left(e^{i\theta}\hat{a}^\dagger\hat{b} + e^{-i\theta}\hat{a}\hat{b}^\dagger\right), \tag{2.12}$$

where $g_{bs}(t)$ is time-dependent coupling rate. Essentially, the Hamiltonian 2.12 describes the coherent exchange of excitation between two bosonic modes. A simulated example of evolution for this Hamiltonian for two cavities with one of them initialized with one photon is shown in Fig. 2.1b.

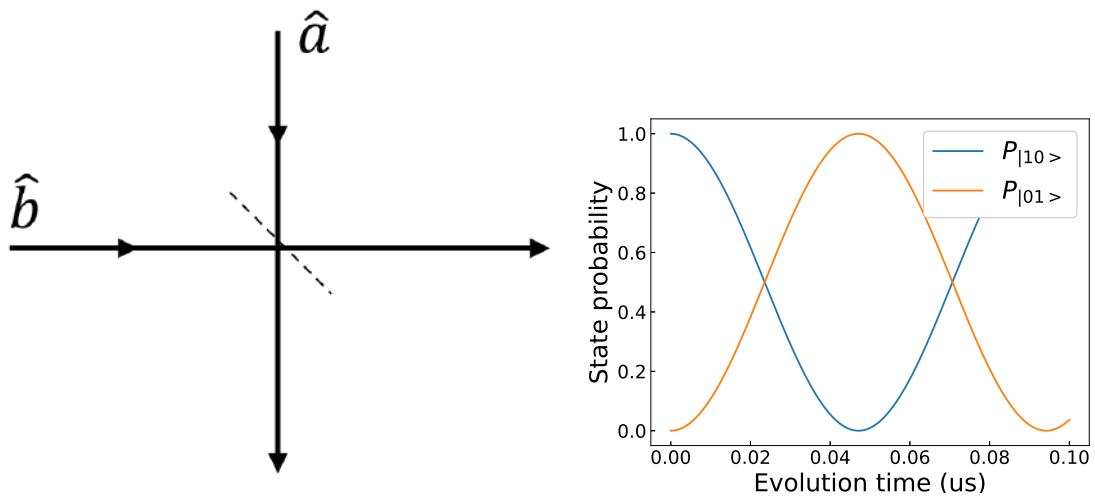

(a) (b)

Figure 2.1: a) Beamsplitting scheme for two bosonic modes passing through a beam splitter. b) Example of population dynamics for two modes with one initially populated with Fock state $|1\rangle$.

2.3.2 Nonlinear coupling

Josephson junction

Manipulating the bosonic modes and forcing them to interact with each other in a controllable way is a challenging process which requires the involvement of a nonlinear element. In superconducting circuits the conventional building block for nonlinear circuits is Josephson junction, which can be treated as a nonlinear inductive element. This structure consists of two superconducting regions that are separated by a weak link, for example an insulating barrier, that permits quantum tunneling of Cooper pairs from one side to the other. [37] This tunneling results in a current across the junction, which depends on the phase difference (φ) of the quantum state wavefunctions on either side of the junction. In series with capacitance Josephson junction composes into a superconducting qubit [16].

SNAIL

First introduced in [29], a SNAIL is a superconducting loop that contains an array of n Josephson junctions with energy E_J connected in parallel with one smaller Josephson junction, which energy is αE_J. The schematic representation is shown in Fig. 2.2.
The potential energy of the element can be written as follows

$$U_{SNAIL}(\varphi) = -\alpha E_J \cos(\varphi) - nE_J \cos\left(\frac{\varphi_{ext} - \varphi}{n}\right), \tag{2.13}$$

where φ is a superconducting phase across the small junction, $\varphi_{ext} = \frac{2\pi\Phi_{ext}}{\Phi_0}$, Φ_{ext}– applied external flux, $\Phi_0 = \frac{h}{2e}$.

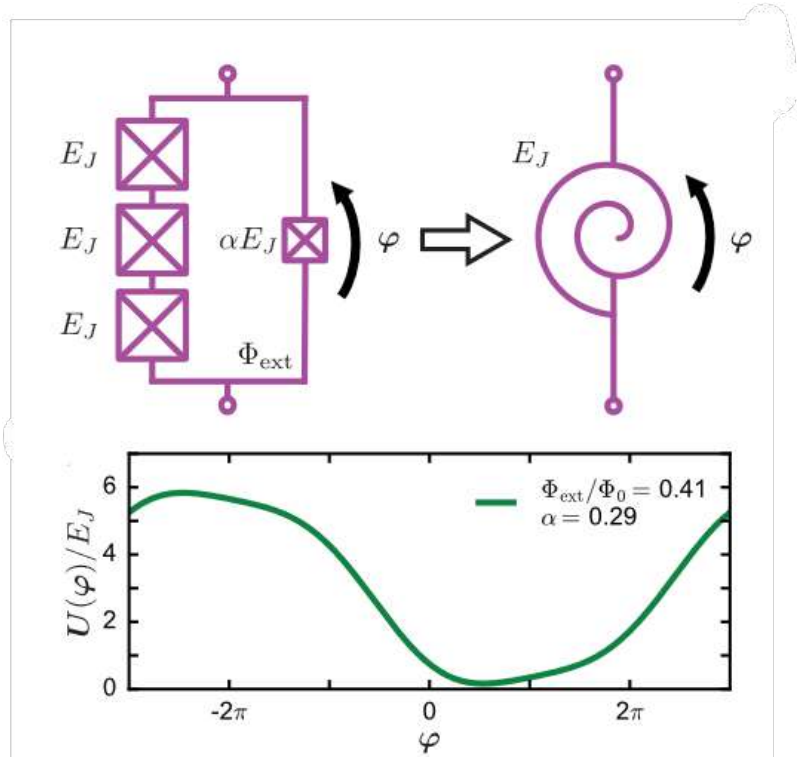

Figure 2.2: An illustration from [29]. (top) a circuit representation of a SNAIL. (bottom) potential landscape of a SNAIL with particular ϕ_{ext} and α. By changing the external flux through the circuit potential energy is modulated.

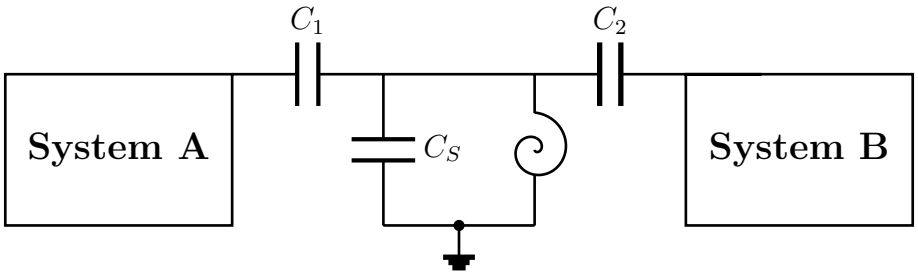

Figure 2.3: Schematic representation of the circuit. The SNAIL coupling element in the center couples two modes a and b.

The SNAIL potential is an asymmetric function with one degree of freedom φ. Due to its design it is possible to precisely tune the external flux in a way to cancel the unwanted quartic-order Kerr interaction terms while maintaining the third-order nonlinear terms to be present. Indeed, one can write the Taylor expansion about the minimum φ_{min} to obtain the effective potential $\tilde{\varphi} = \varphi - \varphi_{min}$

$$\frac{U_{eff}\left(\tilde{\varphi}\right)}{E_J} = c_2\tilde{\varphi}^2 + c_3\tilde{\varphi}^3 + c_4\tilde{\varphi}^4 + ..., \tag{2.14}$$

where $c_1 = 0$ since the minimum is considered. Coefficients $c_1, c_2, c_3, c_4...$ are determined by values n, α and Φ_{ext}.

The ability to modulate a circuit with external flux using a SNAIL and thereby cancel out parasitic fourth-order Kerr terms makes a SNAIL-based coupling element an appealing and promising approach for achieving connectivity implementation.

2.3.3 System Hamiltonian

To implement the beamsplitting gate (eq. 2.12) between two bosonic modes in a controllable way, two linear LC-oscillators need to be capacitively connected to a coupling element, the nonlinear mode, composed of a capacitance in series with a SNAIL, which represents nonlinear inductance. The schematic representation of this system circuit is shown in Fig. 2.3.

Second quantisation of undriven SNAIL potential (eq. 2.13), truncated to the fourth order, yields

$$\frac{\hat{H}_c}{\hbar} = \omega_c\hat{c}^\dagger\hat{c} + g_3\left(\hat{c} + \hat{c}^\dagger\right)^3 + g_4\left(\hat{c} + \hat{c}^\dagger\right)^4, \tag{2.15}$$

where $\hat{c}$ is the annihilation operator associated with the coupler mode, g_3 and g_4 are nonlinearities, which are implicitly functions of the SNAIL circuit parameters.
Hamiltonian of the corresponding circuit system can be written as follows

$$\frac{\hat{H}}{\hbar} = \omega_a\hat{a}^\dagger\hat{a} + \omega_b\hat{b}^\dagger\hat{b} + \frac{\hat{H}_c}{\hbar} + g_{ac}\left(\hat{a}\hat{c}^\dagger + \hat{a}^\dagger\hat{c}\right) + g_{bc}\left(\hat{b}\hat{c}^\dagger + \hat{b}^\dagger\hat{c}\right) + \frac{\hat{H}_d}{\hbar}. \tag{2.16}$$

The first and the second term correspond to Hamiltonians of harmonic oscillators, the third term is eq. 2.15, the fourth and the fifth terms correspond to the capacitive

coupling between neighbouring modes with g_{ac}, g_{bc} – coupling rates. The last term is the drive Hamiltonian.

In the following part of the section, two distinctive approaches for realizing beamsplitting are described.

Parametric coupling

Diagonalizing the harmonic part of the coupler Hamiltonian and substituting the coupler operator with

$$\tilde{c} \longrightarrow \hat{c} + \frac{g_{ac}}{\Delta_{ac}}\hat{a} + \frac{g_{bc}}{\Delta_{bc}}\hat{b}, \tag{2.17}$$

where $\Delta_{ac} = |\omega_a - \omega_c|$, $\Delta_{bc} = |\omega_b - \omega_c|$, the second-order terms in eq. 2.16 are diagonalized.

The drive Hamiltonian corresponding to the flux drive is

$$\hat{H}_d = g_2^{ac}(t)\left(\hat{c} + \hat{c}^\dagger\right)^2, \tag{2.18}$$

which is, with a substituted coupler annihilation operator from eq. 2.17

$$\tilde{H}_d \longrightarrow g_2^{ac}(t)\left(\hat{c} + \frac{g_{ac}}{\Delta_{ac}}\hat{a} + \frac{g_{bc}}{\Delta_{bc}}\hat{b} + h.c.\right)^2. \tag{2.19}$$

Parenthesis expansion of this eq. 2.19 gives us the desired efficient beamsplitting Hamiltonian, similar to the eq. 2.12, with coupling rate

$$g_{bs}(t) \sim g_2^{ac}(t)\frac{g_{ac}}{\Delta_{ac}}\frac{g_{bc}}{\Delta_{bc}} \tag{2.20}$$

time-dependent and thus controllable.

Three-wave mixing

Implementation of a SNAIL element also allows to perform three-wave mixing (3WM). 3WM is the nonlinear interaction, in which two photons are combined to form the third one. This process involves the third-order nonlinearity in potential energy.

A schematic representation of this process is shown in Fig. 2.4a.

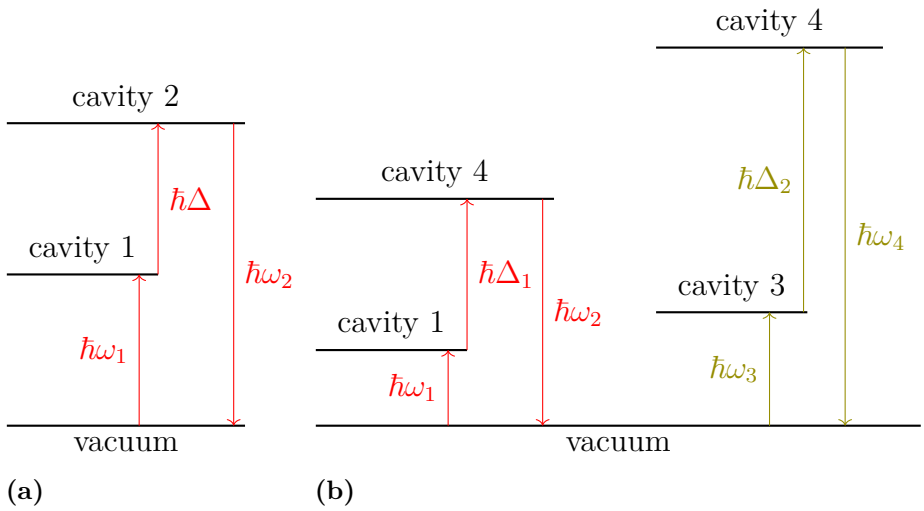

Figure 2.4: a) 3WM. Initial photon populates cavity 1. A pump at frequency difference $\Delta = |\omega_2 - \omega_1|$ is applied to the SNAIL coupler mode. This leads to creation of the third photon with resonant frequency of the second cavity ω_2, while the photon in cavity 1 and one photon from the drive field is annihilated. b) 2×3WM in parallel. It is essential that the resonant frequency differences for the cavities are not degenerate. The designations in the Figure are i) $\Delta = |\omega_2 - \omega_1|$ ii) $\Delta_1 = |\omega_2 - \omega_1|, \Delta_2 = |\omega_3 - \omega_4|$

In principle, both parametric flux coupling and this process of 3WM can potentially run two beamsplitting processes in parallel, involving multiple cavities by applying the corresponding pulses to the coupler simultaneously. However, in this case it is crucial that none of the frequency differences between participating cavities is degenerate. An example of two 3WM processes in parallel is represented in Fig. 2.4b.

The drive Hamiltonian for the charge pulse is

$$\hat{H}_d = F\left(\hat{c} + \hat{c}^\dagger\right). \tag{2.21}$$

This action corresponds to the displacement of the coupler annihilation operator $\hat{c} \longrightarrow \hat{c} + \xi(t)$, where $\xi = \frac{F}{\omega_p - \omega_c} e^{-i\omega_p t}$ with F – amplitude of the drive, ω_p – pump frequency. Substitution of the new coupler annihilation operator to the SNAIL Hamiltonian (eq. 2.15) and taking into account the cubic term gives the effective beamsplitting gate with linear coupler rate

$$g_{bs} \sim \frac{g_{ac}}{\Delta_{ac}} \frac{g_{bc}}{\Delta_{bc}} \frac{F}{\omega_p - \omega_c} g_3. \tag{2.22}$$

3
Design and fabrication

After outlining the general concepts of coupling strategies, the dynamics underlying them, and the potential implementations of beamsplitting gates, the subsequent steps involved designing the planar construction of the chip, defining its parameters, and simulating them. These actions were undertaken in order to subsequently fabricate a device based on the generated design.

3.1 The idea

Taking the inspiration and adapting the design concept from [39], the coupler is considered in two manners (i) a switch that allows to perform the beamsplitting dynamics with in-situ suppressing all Hamiltonain terms that are not participating in the beamsplitting interaction, (ii) a single platform for connectivity of several cavities via parametric coupling and 3WM. These two notions result in a planar architecture with four transmission line cavities interconnected with a single SNAIL coupling element; this architecture is represented in Fig. 3.1.

3.2 Chip components

The planar architecture of the chip was simulated using the Qiskit Metal library in Python. The chip's layout is illustrated in Fig. 3.1. Due to the chip's complex structure, it has been divided into four parts. These are referred to as branches, with the left-most readout+cavity system as branch 1. This branch contains a readout resonator ("res 1" in the Fig. 3.1), a qubit ("qb 1") and a cavity ("cav 1"). The next cavity is referred to as "cav 2," denoted as branch 2.Subsequently, there is cavity 3 labeled as "cav 3," representing branch 3. Finally, the rightmost system composed of "res 4," "qb 4," and "cav 4" is designated as branch 4. By utilizing this labeling scheme, the connections between various elements become intuitively comprehensible and simple to recall.

In this section, the overarching conceptual ideas behind the chip and its constituent elements are discussed. Specific target parameters and the simulation methodology can be found in sec. 3.3.

Termination ports

To insert a chip into a dilution cryostat, it is necessary to place the chip within a sample holder. This arrangement facilitates the proper connection of the chip to

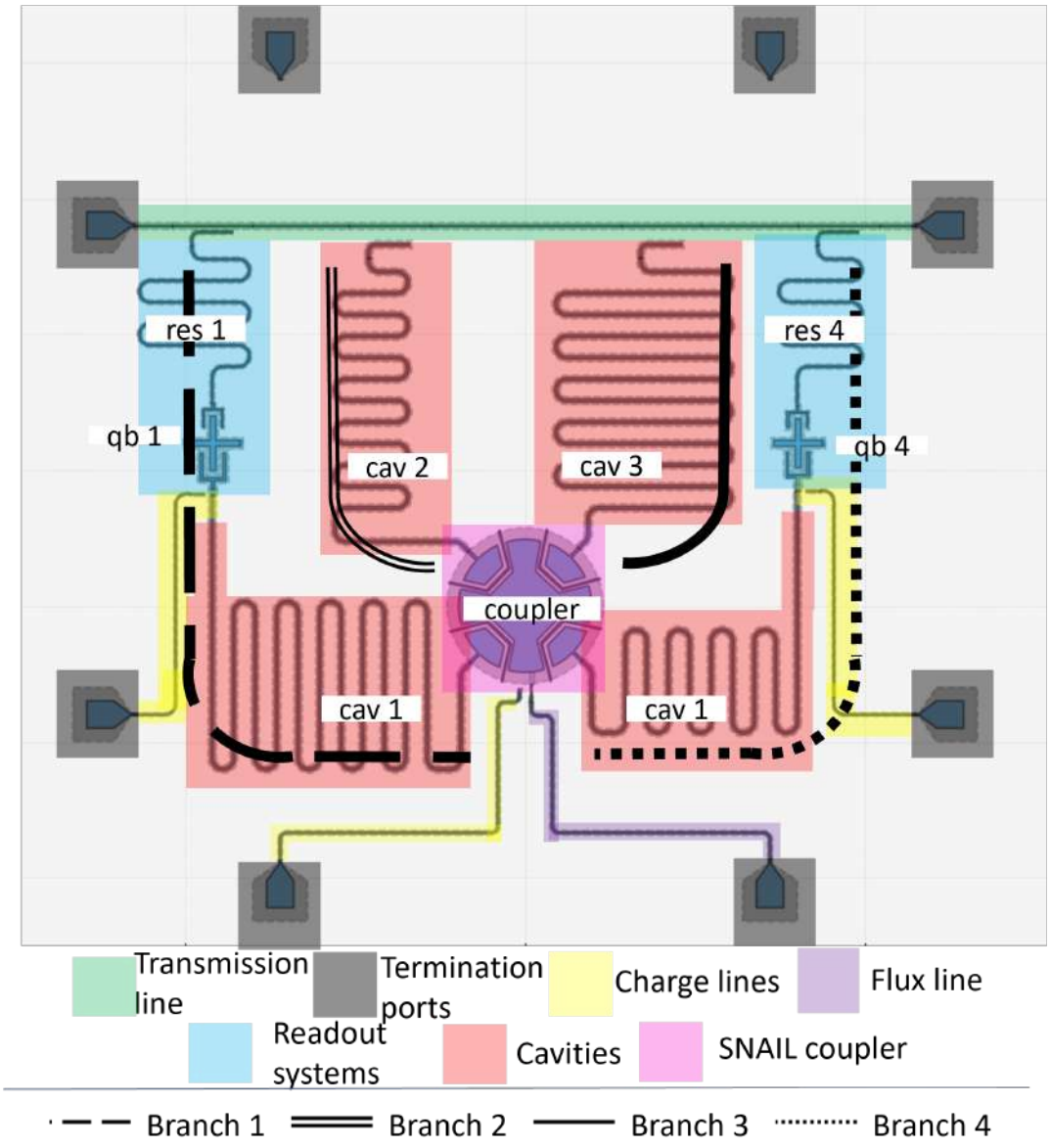

Figure 3.1: Schematic of the chip design in Qiskit Metal render. Termination ports (black) serve as connectors between the sample holder and the chip transmission line (green), charge (yellow) and flux drives (purple). Two readout systems (blue) are coupled to two out of four cavities (red). All cavities are capacitively terminated with the SNAIL coupler (pink).

the hardware components. The sample holder, designed by the 202-Q group [50], imposes certain limitations on the chip size and design. To fit the holder and satisfy the amount of available ports, the designed chip was dimensioned to be 7 mm × 7 mm in size. This chip layout incorporates eight ports that are evenly distributed around the periphery of the chip, as shown in Fig. 3.1 (indicated in black).

Transmission line

Transmission line (Fig. 3.1, green) serves the purpose of propagating microwave pulses to control the readout resonators of the system. This transmission line comprises a central distributed conducting element and an outer ground space.. Both of these components are positioned on a dielectric substrate and are separated from each other by a vacuum gap. To provide the execution of the chip without unwanted signal reflection, the impedance of the output line must have the equivalent impedance with its terminating ports. For impedance of 50Ω the trace width equal to 20 μm and trace gap width equal to 12 μm were taken.

Cavities

Harmonic oscillators that serve as CV quantum state storage are often referred to as "cavities". One can construct a planar architecture of a cavity with a lumped LC-circuit or a distributed coplanar waveguide (CPW) element. The latter case was used to implement cavities in this design (Fig. 3.1, red). Given the disadvantage of limited internal quality factor, this type of resonators are still the most commonly used due to the ease of design for modes up to 10 GHz and on-chip fabrication. In this design, two out of four cavities are directly coupled to the transmission line to avoid frequency crowding.

A CPW resonator is formed by a metal stripe with length d_{res} and width w_{res}, separated from the ground metal plane by a gap s_{res}. Details of the geometry are given in Fig. 3.2. The choice is motivated by the general notion that the target internal quality factor (Q) should be as large as possible. There is empirical evidence on the particular distributed capacitance value that maximizes the internal Q. The geometry parameter choice for cavities is thus dictated by this capacitance value; particular definitions for the strip width and gap are given in the description for Fig. 3.2. All cavities are designed open to ground with $\frac{\lambda}{2}$ boundary conditions.

Readout

The chip contains two readout systems consisting of low-Q readout resonators and dispersively coupled transmons (blue). The resonators are intentionally designed to have a low Q by being overcoupled to the transmission line. This configuration allows information to escape towards the transmission line while preventing leakage to the environment.

In the transmon design, a conventional cross-like shape with a standard width-to-gap

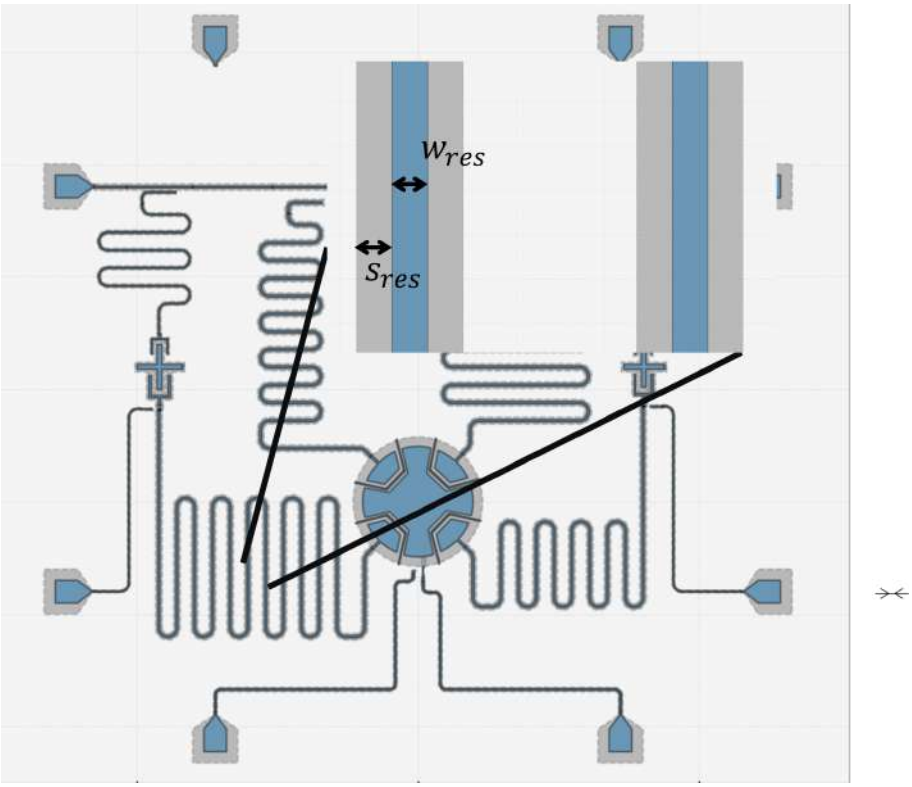

Figure 3.2: A cavity, zoomed CPW image. The defined parameters are as follows: $w_{res} = 20\mu$m, $s_{res} = 20\mu$m for all cavities.

ratio was used. The metallic cross structure contributes to a distributed capacitance, while the Josephson junction is effectively modeled as a rectangular shape positioned at the cross's edge, serving as a termination to the circuit ground. The capacitance of this nonlinear LC-circuit can be tuned by modifying the shape and proportions of the cross. Furthermore, the coupling between the resonator, cavity, and the transmon is adjustable through the parameters of the capacitive coupling claw. Detailed representation of this structure is shown in Fig. 3.3. The qubit charge energy E_C was conventionally chosen to be $E_C = 220$ MHz to keep the the qubits in the transmon charge-insensitive regime $\frac{E_J}{E_C} \ll 1$. Detailed geometry parameters are listed in Table 3.1

The readout resonator coupling to the transmission line is represented in Fig. 3.4. Note that both readout resonators are terminated short to ground with $\frac{\lambda}{4}$ boundary condition.

SNAIL coupler

The coupler (3.1, pink) consists of a large capacitance element. Four cavities are connected to this element through trapezoid-like shapes. The quantity of coupled resonators can be customized based on the circuit's requirements. Metallic stripes located between the cavities and the primary plate serve as planar bridges that link the ground sections of the chip. At the lower part of the coupler, a rectangular shape

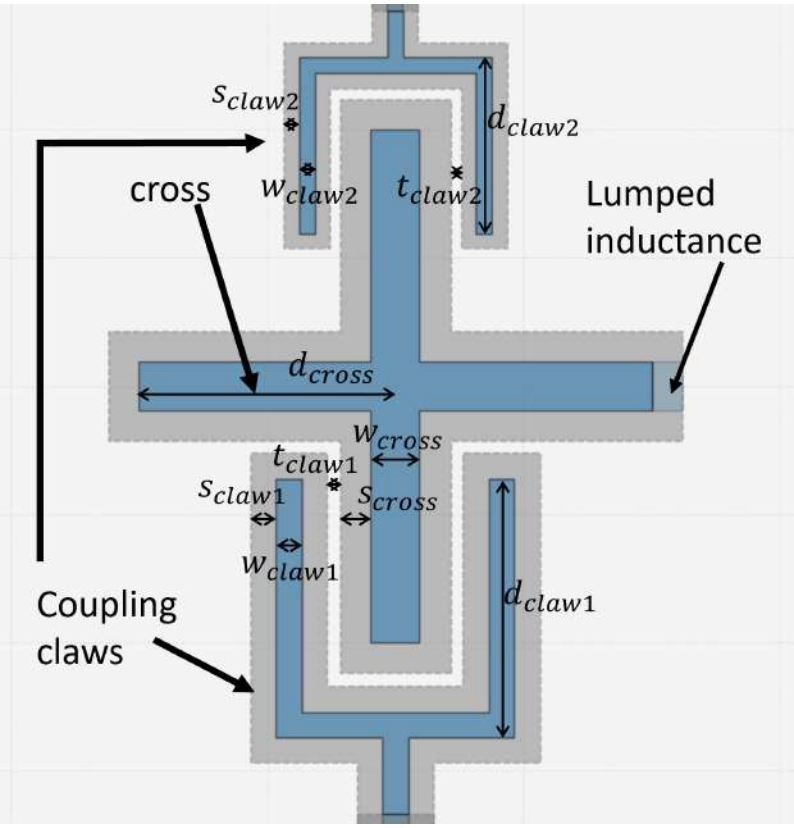

Figure 3.3: A transmon and resonators capacitive claw coupling, zoomed CPW image.

Parameter name	Branch 1 value	Branch 4 value
d_{cross}	200 μm	178 μm
w_{cross}	38 μm	38 μm
s_{cross}	24 μm	24 μm
d_{claw1}	182 μm	160 μm
w_{claw1}	20 μm	20 μm
s_{claw1}	20 μm	20 μm
t_{claw1}	10 μm	5 μm
d_{claw2}	125 μm	112 μm
w_{claw2}	12 μm	12 μm
s_{claw2}	12 μm	12 μm
t_{claw2}	8 μm	11 μm

Table 3.1: Transmon geometry parameters

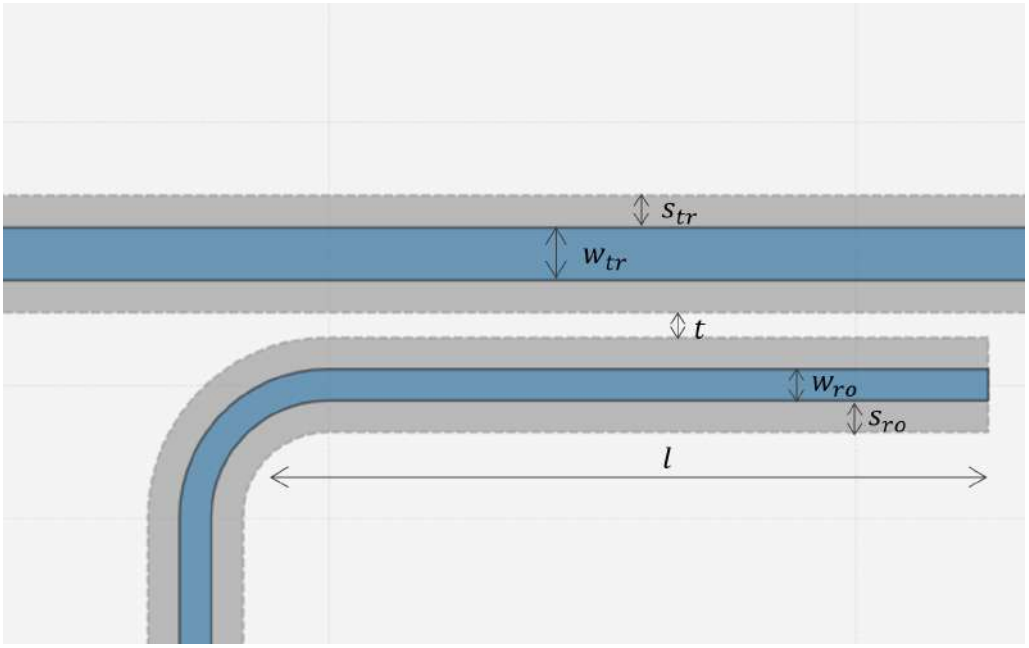

Figure 3.4: A readout resonator coupled to the transmission line, zoomed CPW image. The defined parameters are as follows: $w_{tr} = 20$ μm, $s_{tr} = 12$ μm, $w_{ro} = 12$ μm, $s_{ro} = 12$ μm, $t = 10$ μm, $l = 300$ μm.

concludes the capacitance connection with the ground and highlights the intended location for the SNAIL circuit. In this stage of design, the SNAIL is conceptualized as an effective sheet inductance value. Subsequently, the specific SNAIL parameters are chosen to align with this value. The capacitance of the element can be adjusted by modifying the dimensions of the metallic component. The combined values of capacitance and inductance establish the resonant frequency of the coupler. Detailed schematic is shown in Fig. 3.5.

Charge drives

To manipulate a qubit, a voltage pulse needs to be applied to the qubit drive line, causing oscillations at the qubit's resonant transition frequency. The same charge line can be utilized to displace the state of the corresponding cavity by sending a pulse at the cavity frequency. Lastly, the charge drive is essential for the coupler to implement the described 3WM mechanism. This manipulation is realized by dedicated charge drive lines (Fig. 3.1, yellow, can also be seen in Fig. 3.5). The distance between the charge drive lines and the cavities is 27 μm. The similar distance was chosen for the coupling charge drive line.

Flux drive

To achieve the Kerr-free point, the SNAIL coupler is constantly exposed to the static external flux φ_{ext}^{dc}. This flux originates from a controllable DC voltage, which biases a coil outside the sample holder. This coil is a source of the static external flux. The on-chip flux line (Fig. 3.1, purple) enables modulation of the flux in the form

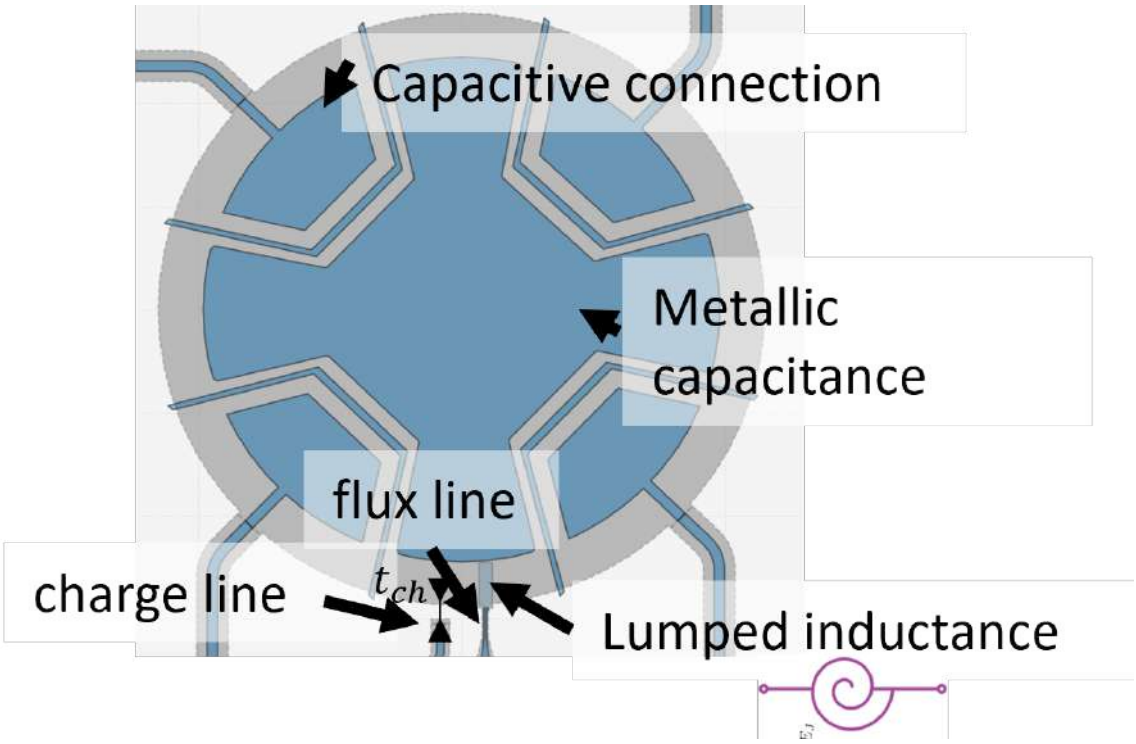

Figure 3.5: A coupler with termination of four cavities. For the charge line $t_{ch} = 27$ μm.

$\varphi_{ext}(t) = \varphi_{ext}^{dc} + \varphi_{ext}^{ac}(t)$. Note, that in order not to activate nonlinearities and to stay at equilibrium, the AC-flux modulation must remain under the condition $\frac{|\varphi_{ext}^{ac}(t)|}{|\varphi_{ext}^{dc}|} \ll 1$ to guarantee the applicability of perturbation theory around the minimum of the potential energy. Flux line is positioned on the distance of 5 μm from the SNAIL circuit.

3.3 Target parameters

The discussion now moves from general notion towards particular values. In this section, the principles of finding proper system parameters and calibrating the design in simulation are shown. The discussion is now transitioning from general concepts to specific values. In this section, the focus shifts towards clarifying the principles of identifying appropriate system parameters and calibrating the design through simulation.

3.3.1 Frequencies

The following considerations were taken into account when selecting element eigenmodes

- In the 3WM process the coupler is driven by a charge drive with a frequency equal to the difference between the resonant frequencies of the target cavi-

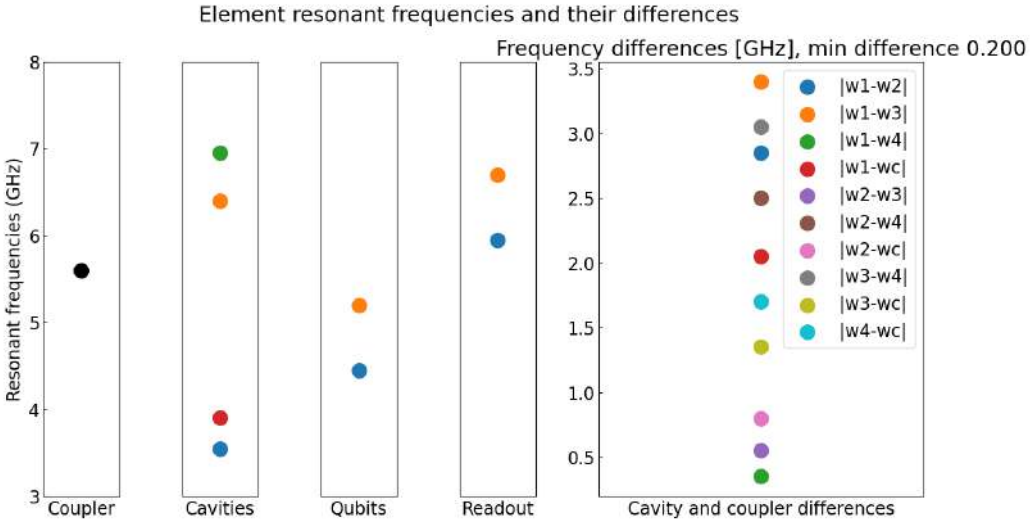

Figure 3.6: A graphical depiction of the target parameters for all chip elements (first four insets) and the comparative list of frequency differences (the fifth inset). With the selected set of system parameters, frequency differences are preserved in a non-degenerate manner. "min difference" refers to the minimum difference between the frequency differences, which belongs to cavities 1 and 4 and is equal to 200 MHz.

ties. To be capable of producing two simultaneous beamsplitter processes, it is essential to maintain non-degenerate frequencies and frequency differences among the cavities. (Fig. 2.4b).

- The readout resonators and the transmons coupled to them must operate in a dispersive regime to enable quantum non-demolition readout with Wigner tomography capabilities.
- Similarly, it is important to maintain the dispersive regime in qubit+cavity systems to ensure the ability of using standard universal control protocols such as SNAP [43] or ECD [41].
- Cryostat setups typically operate within a frequency range of $4-8$ GHz. Incorporating high resonant frequencies (>20 GHz) into the chip design could potentially lead to the excitation of modes within the sample box.

Parameters for the linear elements, i.e. for the readout and cavity resonators, are shown in the second and the fourth insets of Fig. 3.6, differences of the cavity frequencies are plotted in the fifth offset of the same Figure.

The exact frequency values for each element are as follows.

- $\frac{\omega_{c1}}{2\pi} = 3.55$ GHz, $\frac{\omega_{c2}}{2\pi} = 6.95$ GHz, $\frac{\omega_{c3}}{2\pi} = 3.9$ GHz, $\frac{\omega_{c4}}{2\pi} = 6.4$ GHz for cavities in branches 1,2,3 and 4 respectively.
- To keep the cavity+transmon system in a dispersive regime, the inequality $\Delta \gg g$ must remain, where $\Delta = |\omega_{resonator} - \omega_{transmon}|$. Keeping the coupling strength required to be $\chi = \frac{g}{\Delta^2} = 2.5$ MHz, the frequency difference is taken to be $\Delta_1 = 0.9$ GHz for the first branch and $\Delta_4 = 1.2$ GHz for the fourth

branch, with resulting transmon target freuqencies $\frac{\omega_{Q1}}{2\pi} = 4.4$ GHz for branch 1 transmon and $\frac{\omega_{Q1}}{2\pi} = 5.2$ GHz for branch 4.

- To ensure the dispersive readout, the eigenmodes for the readout resonators should be substantially distinct from the transmons. Therefore, the difference is chosen to be $\Delta = 1.5$ GHz for both branches, with following frequencies $\frac{\omega_{r1}}{2\pi} = 5.9$ GHz and $\frac{\omega_{r4}}{2\pi} = 6.7$ GHz for branches 1 and 4 respectively.
- The frequency of the SNAIL coupler is selected to be intermediate between the frequencies of the cavities and significantly distant from each of them (Fig. 3.6, first inset). Adhering to these criteria, the chosen coupler frequency is $\frac{\omega_C}{2\pi} = 5.6$ GHz at Kerr-free point.

3.3.2 Coupling strength

To determine the appropriate coupling rate between cavities and the coupler, two considerations must be taken into account. First, the rate of beamsplitting is directly proportional to the extent of hybridization between the cavities and the coupler. To ensure fast and rapid beamsplitting, it is desired to establish strong coupling between the modes. On the other hand, by coupling to a nonlinear element the linear modes inherit its nonlinearity as well as decoherence and dephasing rates. Therefore, one must choose the coupling in a way that the cavity coherences are not significantly deteriorated. Thus, diminishing the intensity of the cavity-coupler coupling strength would lead to a reduction in the inherent nonlinearity and induced decay/dephasing, yet it would also result in interactions taking place at lower speed. From [39], the decay rate that a cavity inherits from a coupler yields

$$\kappa_a \sim \frac{g_{ac}^2}{\Delta_{ac}^2}\gamma_c, \tag{3.1}$$

with $\gamma_c = \frac{1}{T_{1c}}$ – relaxation rate of the coupler, $\Delta_{ac} = \omega_a - \omega_c$ – frequency difference between the cavity and the coupler, g_{ac} – cavity-coupler coupling rate. Based on the measurements obtained from previous experiment in similar device [49], the authors of [39] chose the coupling rate to be $g_{ac} \sim 100$ MHz. In this research, a similar value was chosen.

The selection of the coupling strength between the qubit and cavities is determined by aiming for maximum state visibility. In this scenario, the dispersive shift between the readout and the transmon should be set as $\chi = \frac{\kappa}{2}$, where κ represents the resonator linewidth and is obtained as the full width half maximum value in the resonator's S_{21} spectrum. As a result, the choice of the readout dispersive shift is $\chi = 300$ kHz.

3.3.3 SNAIL element

As it was discussed in Theory section, a SNAIL element is characterized by several parameters that dictate its operational behavior. These parameters are the number of Josephson junctions n in the loop, the Josephson energies relation α, the

number of large junctions in the shunting array M. Accurate adjustment of these parameters enables the cancellation of undesired Kerr nonlinearities while keeping the third-order terms enhanced, which are involved in 3WM-induced beamsplitting. The following text contains comments on each of these parameters.

- With $n = 1$ Josephson junctions a SNAIL element turns into an asymmetric DC-SQUID, which gives $c_3 = 0$ from eq. 2.14 SNAIL representation. [47] On the other hand, with $n \gg 1$ a SNAIL starts behaving as an inductance and the potential reaches the fluxonium qubit limit. [48] Thus, the proper lower limit is $n \geq 2$. Additionally, in paper [39], it is noted that when $\alpha < \frac{1}{n}$, a single minimum in the SNAIL potential landscape is present. Therefore, to prevent the occurrence of multistability, it is crucial to operate within the regime that satisfies this inequality. The authors also emphasize that choice of n affects the ratio $\frac{c_3}{c_5}$ of coefficient of SNAIL potential Taylor expansion. The correspondence is $\left|\frac{c_3}{c_5}\right| = \frac{n^2}{n^2+1}$. To attain favourable ratio of the desired c_3 and unwanted c_5, maximum suppression of unwanted fifth-order interactions, the choice $M > 2$ is reasonable. In Chalmers Myfab cleanroom a $n = 3$ SNAIL element had been successfully fabricated before. In this chip, a $n = 3$ SNAIL element is inserted as well, led both by the theoretical restriction and fabrication considerations.
- Josephson energy relation α determines the shape of SNAIL energy potential landscape. To achieve a Kerr-free point at a specific frequency, which corresponds to the point where the derivative $\frac{\partial \Phi}{\partial \omega}$ attains its maximum value, it becomes essential to determine the appropriate value of α. This ensures that the curve of the SNAIL potential intersects the desired frequency at the Kerr-free point. For the chosen target SNAIL coupler frequency corresponding $\alpha = 0.133$.
- Number of SNAILs. In the paper [39] the authors have tested several devices with $M = 3$ SNAILs in an array and observed their remarkable ability to effectively mitigate quartic interactions. Nevertheless, their effectiveness was hindered by an unintended connection between the powerful beamsplitter pump and the transmons utilized for oscillator control. Furthermore, the experimental setup in this thesis involves the flux drive of the SNAIL coupler. If multiple SNAILs were incorporated into the coupler design, it would lead to an escalation in chip complexity, as each individual SNAIL would require equal and simultaneous driving.. Therefore, it was decided to fabricate a SNAIL circuit with $M = 1$ number of elements.

Qiskit metal has limitations on modelling quantum mechanics of Josephson junctions. Hence, implementation of nonlinear circuit elements utilizing this library is not feasible. Instead, to indicate the approximate position and effective inductance, non-linear junctions are simulated as rectangles with effective inductance values, which are specified in the code for simulation. This effective inductance value should correspond to the inductive value of nonlinear elements. For SNAIL, it should correspond to the value at the flux point of interest. Hence, a nonlinear element can be observed as an LC-oscillator with distributed capacitance and compact inductance.

Essentially, the equation

$$f = \frac{1}{2\pi\sqrt{LC}} \tag{3.2}$$

allows to manually obtain the coupler eigenmode. An automatic method for evaluating frequencies is discussed in the next section.

3.4 Simulation

After determining the system parameters and establishing the chip's topology, the next step involves customizing the geometry of all elements to align with the designated target frequencies and coupling strengths. For this purpose, the Ansys High-Frequency Structural Simulator (HFSS) software was utilized. This software is specifically designed for the simulation of complex objects, and it was used with the generated Qiskit metal CPW design.

pyEPR simulation

Energy-participation ratio (EPR) method provides a powerful tool for quantum chips characterization based on circuit geometry. It also allows to take into account material composition. [51] Qiskit Metal utilizes a Python library pyEPR, that allows to perform circuit simulations based on the EPR method. The simulation of system frequencies and coupling rates is performed via EPR analysis, executed through a script. With this method, all element frequencies, qubit-cavity and qubit-readout coupling strengths are obtained.

LOM analysis

However, automated pyEPR method of analysis could not manage to estimate the coupling rate between the cavities and the SNAIL coupler. To account for coupling strength, another approach is used, which is to find the numerical value manually utilizing the following equation

$$g = 0.5\frac{C_{coupling}}{\sqrt{C_{qubit} \cdot C_{res}}}\sqrt{\omega_{qubit} \cdot \omega_{res}}, \tag{3.3}$$

where $C_{coupling}$ is the coupling capacitance between the mode and the coupler, C_{qubit} is replaced by the coupler self-capacitance and C_{res} is the resonator self-capacitance. The capacitance values are defined via lumped oscillator model (LOM) analysis. Once the capacitance matrix is obtained, it is possible to evaluate the coupling rate value.

3.4.1 Spurious mode

A challenge that arose during high-frequency simulation is illustrated in Figure 3.7 (top panels). The electromagnetic field, which corresponds to a specific mode, is anticipated to be confined within the considered CPW element, as the distribution

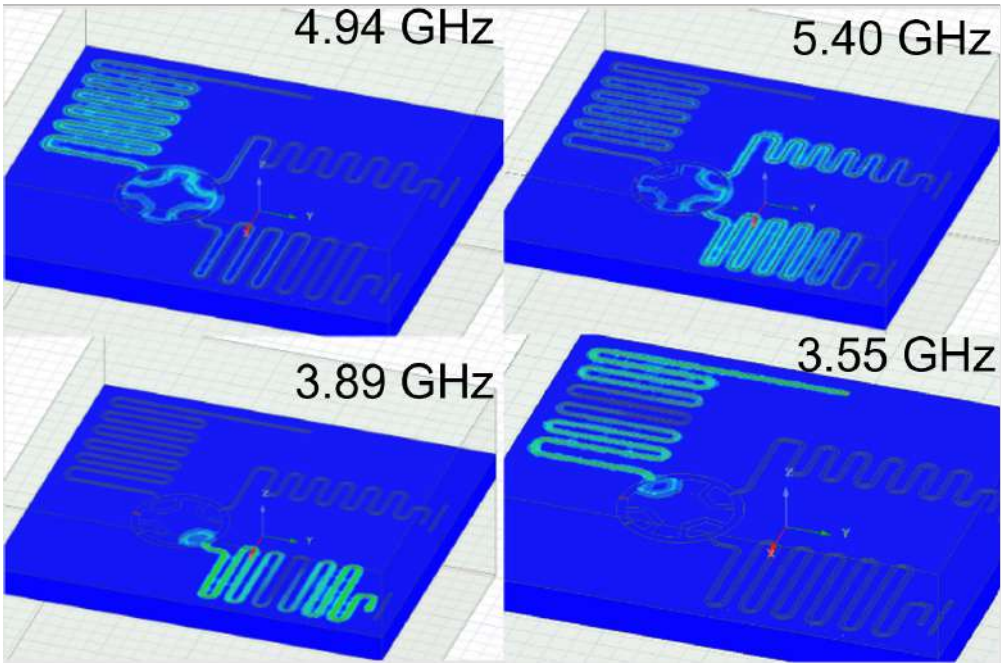

Figure 3.7: Electro-magnetic field distribution of the circuit. The spurious mode appearance in HFSS simulation is illustrated. As one can see, the electro-magnetic field of the highest modes tends to "leak" to the other elements.

shown in Fig. 3.7 (bottom panels). However, at higher frequencies, there is observed "leakage" of the field into the connected CPW structures. This distribution is such that it compromises the isolation of various components.

To exclude the possible occurrence of unaccounted circuit, a lumped-element reconstruction of the chip was performed. The Microwave Office software was used to represent the circuit model and build S_{21} spectroscopy. This circuit with the explanation on its elements correspondence to the chip scheme is shown in Fig. 3.8.

However, this lumped-element simulation has not shown the undesired mode. The resulting S_{21} spectroscopy is represented in Fig. 3.9 . As one can see, the resulting spectrum consists of the eigenmodes of the left cavity (modelled as a transmission line TLIN1), the coupler LC-oscillator, and the right cavity TLIN2, respectively. The fourth mode, denoted by the asterisk, represents the double frequency of the resonator with the lowest frequency.

To deal with this problem, air bridges have been introduced into simulation. It is a necessary implementation to mitigate electromagnetic field modulation, thereby preventing undesired mode appearance within the ground plane. An API which allows drawing the airbridges directly in HFSS via the same script that renders the CPW configuration was used. This implementation allowed to get rid of the spurious mode in the simulation and decrease the “leakage” of the other modes to the coupler. The resulting picture of electro-magnetic field distribution after air bridges implementation is shown in Fig. 3.10.

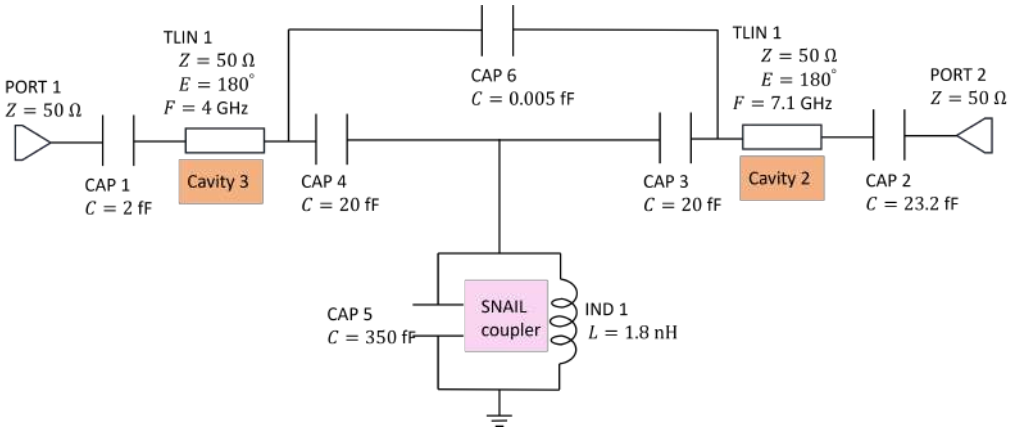

Figure 3.8: Circuit model of the chip part. Two transmission lines, which indicate the corresponding CPW resonators, are capacitively terminated with ports. Each of them are coupled to the coupler, represented by an LC-circuit at the bottom of the cartoon, as well as to each other. The coupler is terminated to ground. The capacitance values for CAP6 and CAP3 are calculated via LOM simulation in HFSS. CAP4 is equal to CAP3. CAP1, CAP2, and CAP6 are chosen with the notion that these capacitances are considerably smaller than the simulated values, reflecting the undercoupling of the cavities to the transmission line.

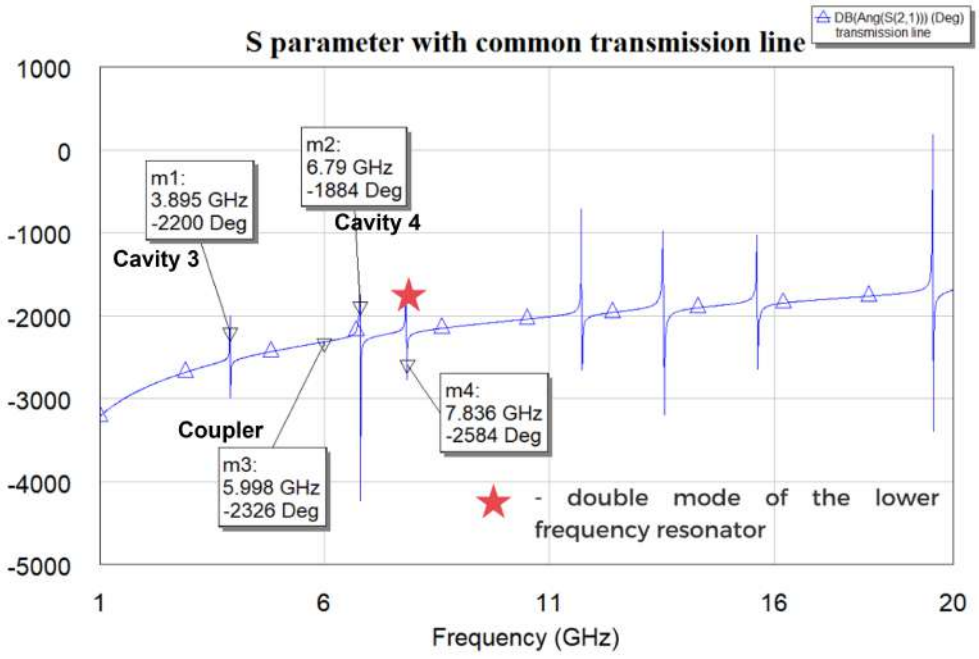

Figure 3.9: S parameter of the circuit. The dips correspond to the eigenmodes of the left cavity, coupler LC-oscillator and right cavity, respectively. The fourth mode, indicated by star, is the double mode of the lowest-frequency resonator. Y-axis represents phase angle in dB.

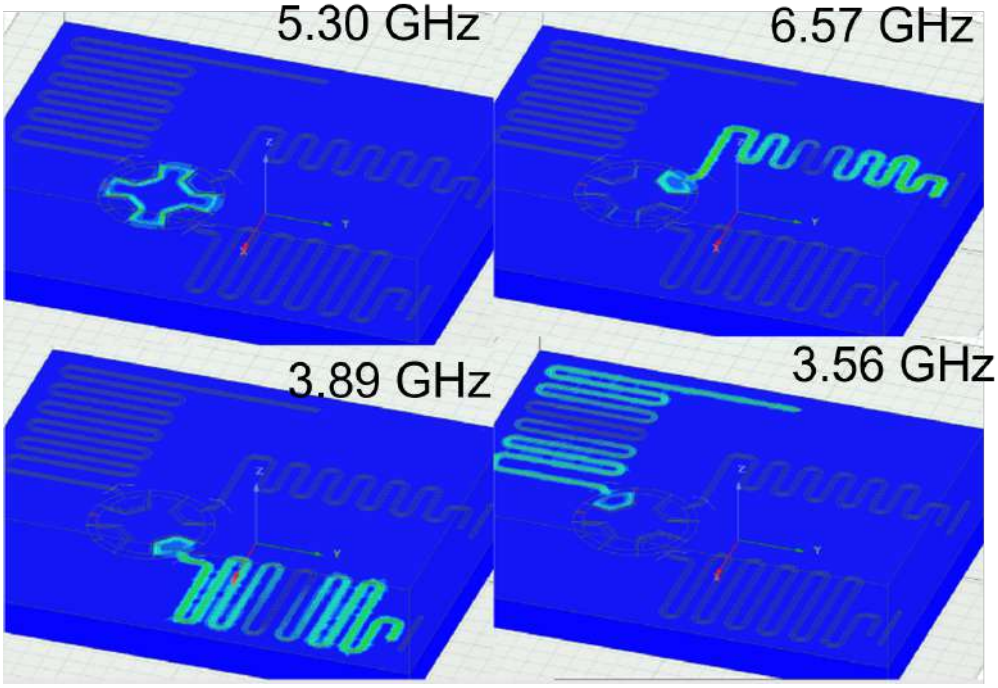

Figure 3.10: Electro-magnetic field distribution of the circuit after air bridges implementation. The spurious mode has disappeared.The resonator modes exhibit field concentration at the capacitive ends of the CPW, as expected. The coupler mode, on the other hand, is predominantly localized at the periphery of the coupler body.

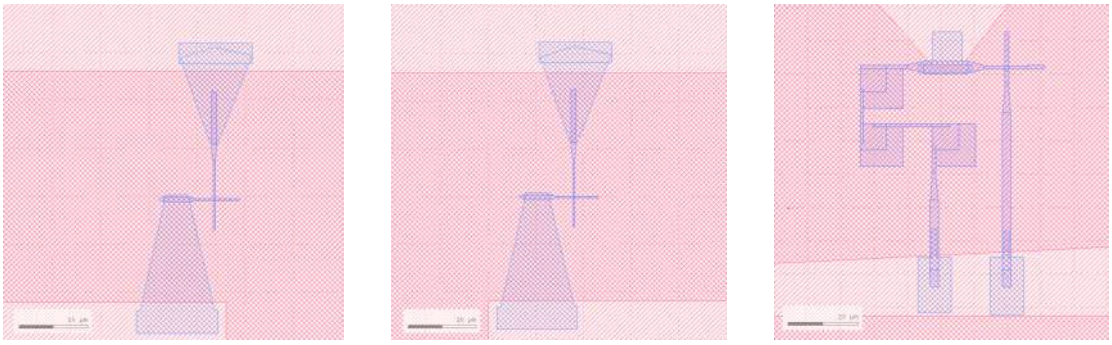

(a) **(b)** **(c)**

Figure 3.11: Klayout sketch of a) Josephson junction for transmon qubit of branch 1 b) Josephson junction for transmon qubit of branch 4 c) SNAIL

3.4.2 Fabrication and post-fabrication

After the design has been accomplished, a Graphic Data System (.gds) file is rendered based on the Qiskit metal layout. Then, using KLayout software, specifications are indicated, particularly the shape and position of non-linear elements, i.e. two Josephson junctions (Fig. 3.11a and 3.11b) of the transmons and the SNAIL element (Fig. 3.11c) of the coupler. The geometry of the non-linear elements is defined based on the designed inductance value used for eigenfrequency simulation as well as empirical calibration curves from previous fabrication rounds.

The structure of Josephson junction requires consecutive deposition of a superconducting layer, a dielectric and again superconductor. The resulting KLayout sketches of Josephson junctions for both transmons and SNAIL are represented in Fig. 3.11.

Once the nonlinear elements are placed, flux trapping holes and dicing detection markers are added, air bridges are depicted and the design is labelled with a unique identifier, the chip is prepared for the fabrication process. The final layout can be seen in Fig. 3.12.
The fabrication of the chip is done in Chalmers Myfab cleanroom facility. Sapphire is used as a substrate with aluminium CPW elements and Josephson junction made via sequential deposition of aluminium, aluminium oxide Al_2O_3 and again aluminium.

3.4.3 Concerns

During the fabrication, the airbridges that were connecting the ground planes collapsed. To fix the situation the ultrasonication technique was used in order to remove the collapsed metal. Following the mentioned procedure and subsequent cleaning steps, manual wire bonding was carried out around the coupler and cavities. This was performed to mitigate the occurrence of extended current paths in the ground plane, which could lead to the unwanted appearance of modes. However, these additional steps within the fabrication might have deteriorated the quality of particular chip elements.

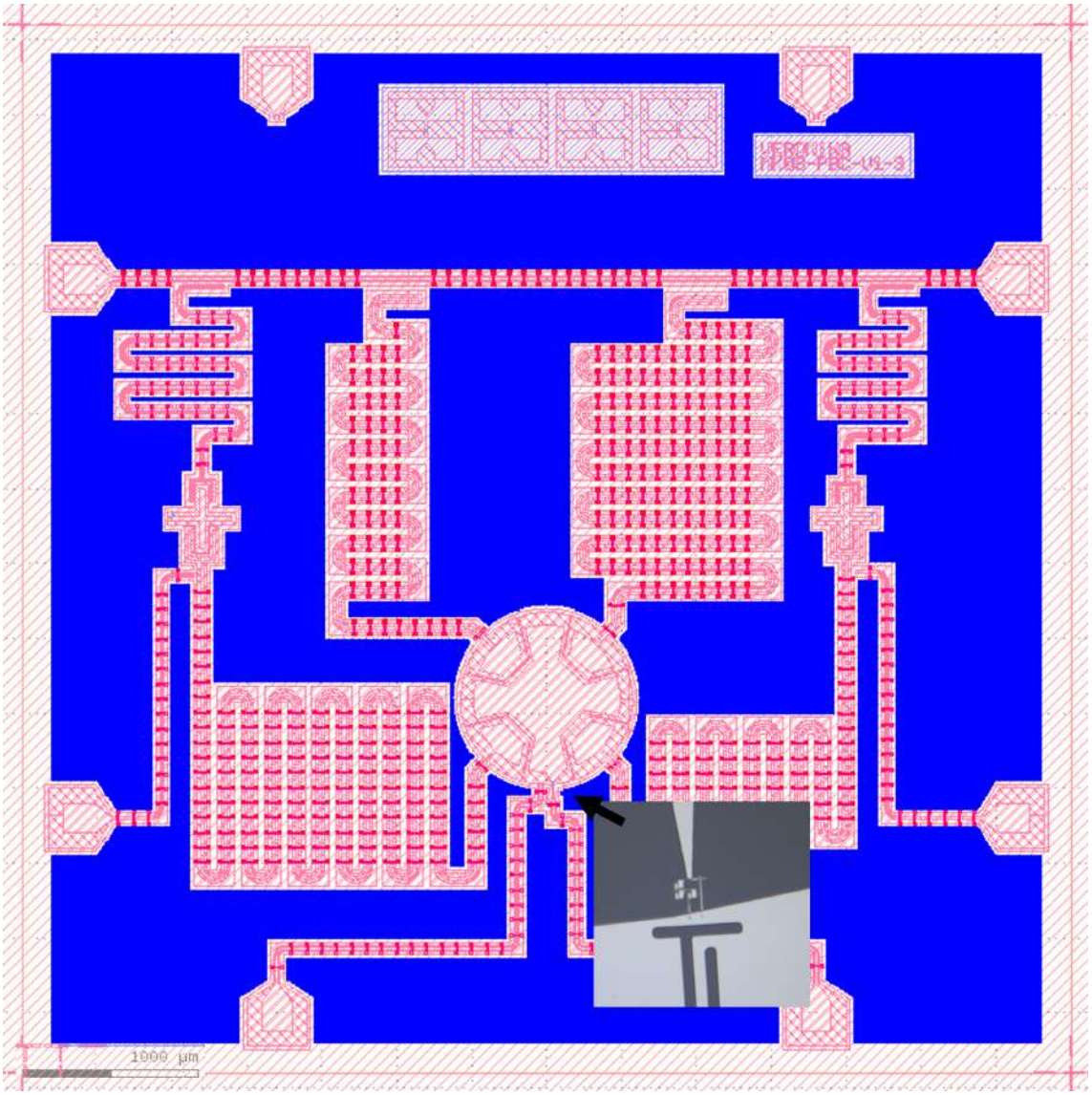

Figure 3.12: The full KLayout chip design. The inset displays an optical micrograph depicting the precise positioning of the SNAIL element after the fabrication process (picture has been taken for the second fabrication round)

Another concern is related to the intention of the operating regime of the SNAIL. The desired operating regime is to have the target frequency 5.6 GHz the Kerr-free point, However, during the design of the SNAIL junctions, the junction sizes were accidentally designed so that the coupler mode takes the target value at the sweet spot (zero external flux).
After the fabrication and dicing it is necessary to glue the chip to a printed circuit board (PCB) and bond the ground (GND) plane and ports to the PCB outputs. This bonding operation was executed using an automated bonding machine. Once the bonding and the subsequent attachment of the PCB to the sample holder were completed, the chip was prepared for immersion into the dilution refrigerator.

4

Experiment

To effectively utilize the designed superconducting chip, it needs to be integrated into a cryostat operating in the millikelvin temperature regime. The discussion on setup preparation is provided, followed by the detailed beamsplitting experiment description.

4.1 The setup

4.1.1 Dilution cryostat setup

Superconductive nature of the designed circuit requires extremely low temperatures in order to achieve the desired operation regime. Thus, the following characterisation and experiment with the fabricated device is done in the cryogenic Bluefors LD dilution refrigerator. The structure of the used cryostat operating at 10 mK is shown in Fig.4.1.
As one can see, the cryostat is divided in sections by plates, each of those is connected to different parts of the thermal circuit inside the cryostat. This separation is needed for placing and sequential thermalization for different parts of the wire circuit that connects the room-temperature operable hardware to the input ports of the chip. Going upside down, the temperature drops, starting from a 50K-plate (cannot be seen in the Fig.) to the base plate, which is placed below the mixing chamber and reaches the lowest temperature of a few millikelvins for a base plate. The chip is mounted below the base plate, the wiring circuit of the setup inside the cryostat can be seen in Fig. 4.2 (bottom).

The structure of the wiring diagram and attenuation distribution is due to the necessity of suppressing the thermal noise: going from room-temperature through intermediate temperatures down to the millikelvin regime, the input from the hardware is attenuated according to the cooling power. If the attenuation is too large compared to the cooling power, this reversibly puts the system towards heating since very high power pulses are required. On top of the device an inductor coil with bias controlled via a script is installed. This coil allows to adjust static magnetic flux through the device coupler which in turn controls the coupler's frequency and hence makes it possible to tune the SNAIL coupler to the Kerr free point.

In dilution cryostat, a combination of different shielding systems is provided. The isolation from microwave photons in the mixing chamber is done by mounting the

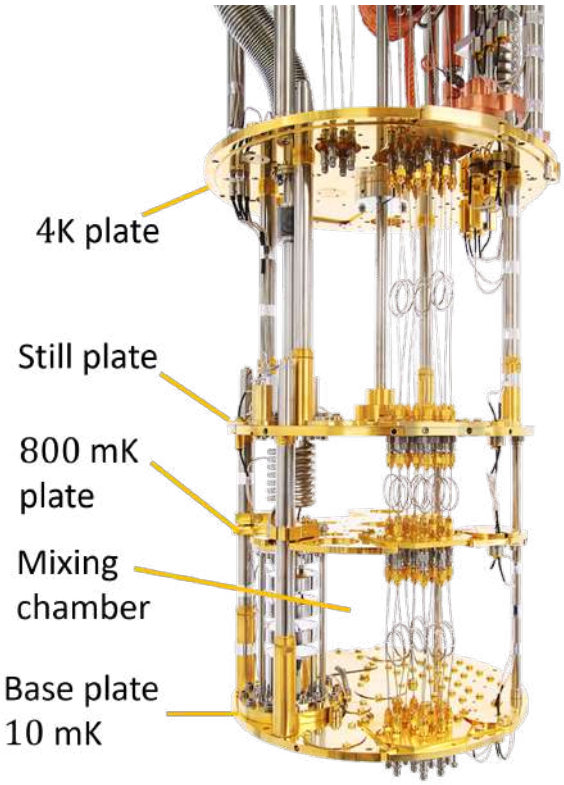

Figure 4.1: Bluefors LD250 ("Wampa") cryostat setup.

device in a copper shield, while a mu-metal high permeability shield protects from the external magnetic field. Another mu-metal shield is implemented to the cryostat below the mixing chamber.

4.2 Characterization

Once the chip is set up in the cryostat, before carrying out the main experiment it is necessary to characterize the device in order to precisely know the essential device parameters and to compare them with the target ones. In case of this research, the characterization was done with two different hardware equipment. The first is vector network analyzer (VNA), which operates in continuous-wave mode and was used for rough characterization of the readout resonator, transmon and coupler frequencies. The second machine is Presto and the time domain measurements were performed.

4.2.1 Frequency domain measurements: VNA

To obtain information about the eigenmodes of the readout resonators and transmons, as well as the readout resonator quality factor (Q) and the qubit anharmonicity coefficient (α), spectroscopy measurements need to be performed. In this research, these measurements are carried out within a continuous-wave framework. The setup involves connecting the input and output of a Vector Network Analyzer

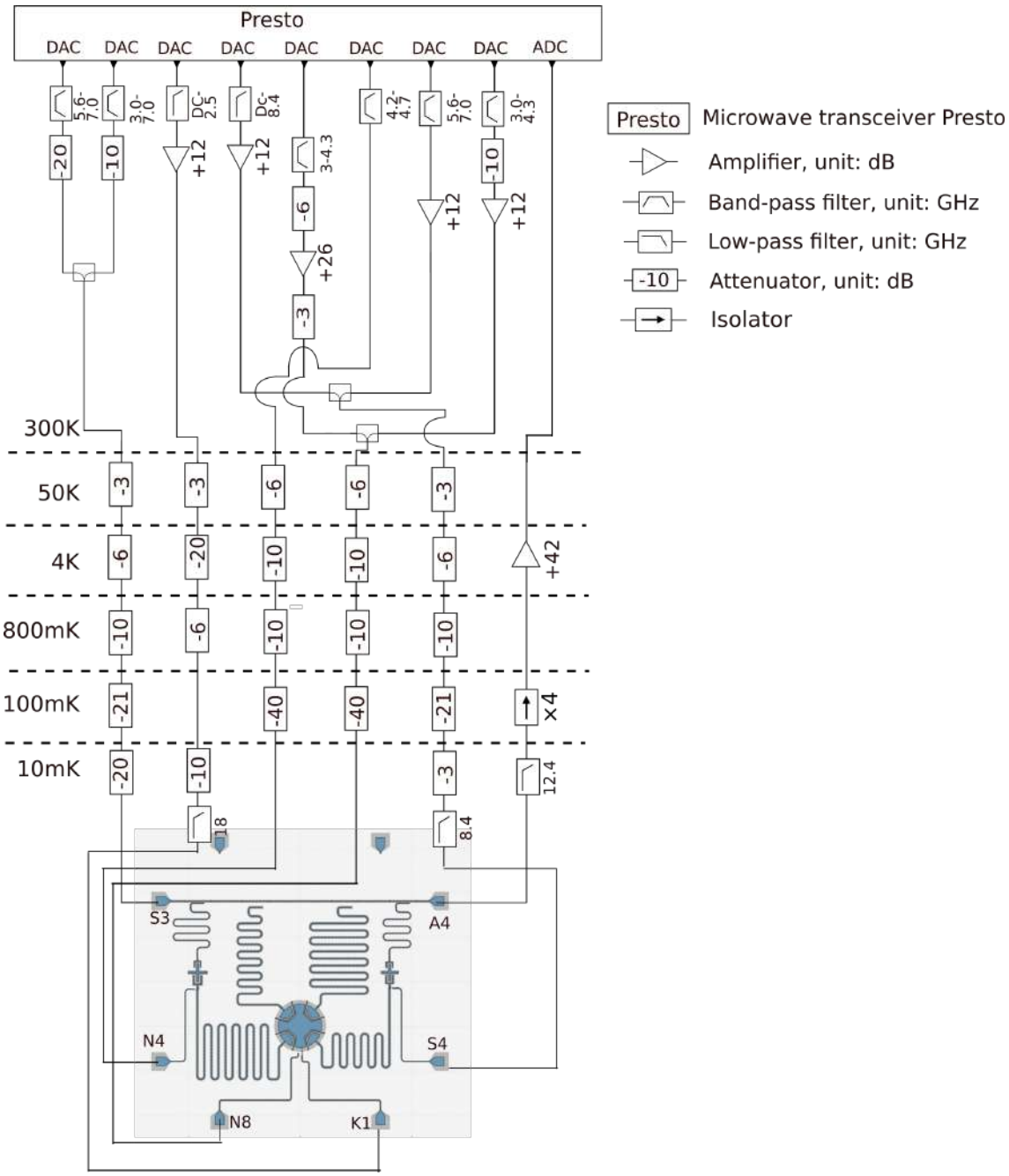

Figure 4.2: Wiring diagram of the setup. Bottom section of the image indicates the connectivity between the sample holder ports and the cryostat wires. Subsequently the attenuation scheme within the cryostat is depicted. Top section represents the hardware setup connections.

(VNA) to the chip's transmission line using coaxial cables. The output port is linked to port $S3$, while the input port is connected to port $A4$ of the cryostat, as shown in Figure 4.2. This configuration is suitable for performing one-tone spectroscopy. However, the VNA has limitations in terms of the number of available ports. Furthermore, it is capable of generating only a single pulse at a time. Therefore, to perform two-tone spectroscopy, a separate local oscillator (LO) source must be used. This type of spectroscopy can be conducted using either (i) two pulses, one for the resonator and another for the qubit pump, both applied to the transmission line, or (ii) a pulse delivered through the qubit's charge drive line, instead of manipulating the qubit via the transmission line. With one-tone spectroscopy the information about resonator frequency and Q is reached, while two-tone gives the qubit's frequency and α.

Before switching from one- to two-tone spectroscopy, it is reasonable to validate whether the qubit is «alive». One possibility for this is performing the punchout measurement, in which one sweeps the power of the resonator signal. The dispersive regime approximation remains valid for a limited number of photons within the resonator. This number is, in turn, determined by the amplitude of the pulse. For low-amplitude pulses, the resonator spectrum indicates the dressed frequency of the readout. Above this limit, the presence of the qubit no longer affects the frequency of the cavity and thus one observes the bare frequency, i.e. the shift in the spectrum equal to χ.

During the VNA measurements, the frequencies of two readout resonators, two transmons, and one cavity were identified and analyzed. Unfortunately, it was not possible to observe one of the directly coupled frequencies (referred to as "cavity 3"). This lack of observation is likely due to the frequency being undercoupled.

To characterize the SNAIL-coupler, specifically to plot the frequency dependence concerning applied external flux, a series of sequential two-tone spectroscopy experiments were conducted. These experiments involved varying the flux while treating the coupler as a qubit. Detailed experiment description and their results are provided in Appendix.

4.2.2 Time domain measurements: Presto

4.2.2.1 Presto framework

Presto is a digital microwave platform [45], that allows to perform complex experiments due to high level of synchronization of output lines and large microwave frequency range (up to 9 GHz). The pulses generated by Presto are digitally synthesized, which significantly simplifies experiments for flux-tunable systems. This is because there is no requirement for the calibration of physical mixers. Presto is operated through a Python-written object-oriented programming interface.

4.2.2.2 Microwave pulse generation

To manipulate the chip elements (displace cavities, populate qubits, etc.) the hardware has to be capable of creating microwave frequency range voltage pulses of controllable length and shape. In order to manage the envelope of voltage pulses, an arbitrary waveform generator (AWG) can be used. However, the sampling rate of this device is very limited and does not allow to generate pulses in GHz range. To perform an output with controllable carrier frequency, AWG signal is multiplied with a continuous LO field.

Multiplying the fields using IQ-mixer, it is possible to perform up-conversion for the signal carried by I and Q ports to RF output signal for device operation and manipulation; and down-conversion of the RF input signal down-converted to the IF frequency understandable for Presto for further hardware analog-to-digital conversion and processing.

Up- and down-conversion is typically done by analog mixers in presence of a separate local oscillator. However, this approach is not ideal, since analog mixers suffer from leakage. Moreover, local oscillators are not good for frequency sweeping, which is essential for spectroscopy, because it is challenging to calibrate them.

The remarkable feature of Presto is that it produces fully-digital up- and down-conversion. The pulses and mixers are defined either via Python API designed for Presto or in a Python setup script directly.

4.2.2.3 Pulsed mode experiment configuration

The configuration of the device requires up to 5 output lines (transmission line $S3$, charge drive lines $N8, S4$ and $N4$, flux line $K1$), 1 input line (transmission line $A4$) and one DC bias output (flux source) to be inserted simultaneously. Presto has 16 RF synchronous output ports, 8 of which are high frequency range (up to 9 GHz). Due to the specification of the designed device the setup is confined to the 8 medium frequency ports available. These output ports are in turn splitted into two groups: tile 1 for ports 1-4 and tile 2 for ports 5-8, each of them has to have one digital-to-analog (DAC) mode and one specific sample frequency. The Presto setup is specified in experimental parameters in the Python file, the setup is shown in Listing 4.1.

```
PRESTO_PULSED: {
        "ext_ref_clk": True,
        "dry_run": False,
        "address": "192.0.2.53",
        "adc_mode": AdcMode.Mixed,
        "adc_fsample": AdcFSample.G2,
        "dac_mode": [DacMode.Mixed02, DacMode.Mixed02,
        DacMode.Mixed02, DacMode.Mixed02],
        "dac_fsample": [DacFSample.G8, DacFSample.G10,
        DacFSample.G8, DacFSample.G8],
        "force_config": True
    },
```

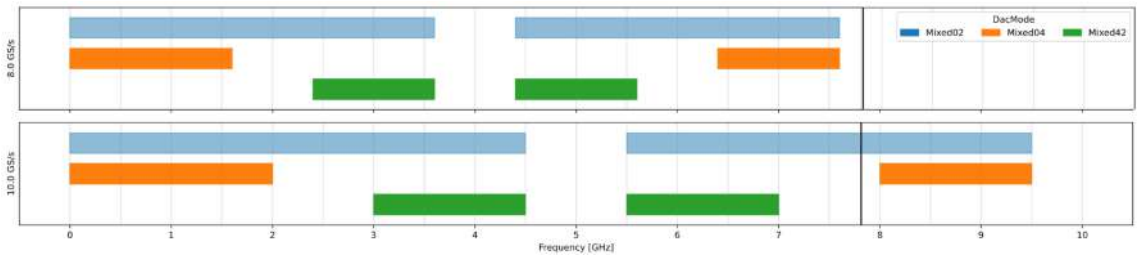

Figure 4.3: Sampling frequency vs output frequency. Blue stripes highlight the available output frequency range

Listing 4.1: Output ports setup

In this Listing one can see, that for the output ports there are four DacModes ("dac_mode") and one-to-one corresponding DAC sampling frequencies ("dac_fsample"). In this setup, only the first two groups, which represent the two tiles of high frequency output ports discussed above, are used. Thus, for both tiles the DacMode Mixed02 is used, for the first tile the corresponding sampling frequency equal to 10 GS/s is chosen, while for the second tile it is 8GS/s. For the second tile, the lower sampling rate is used due to limitations of the hardware. Indication of the specific combination sampling frequency vs DacMode leads to a specific frequency range available for output generation. This ranges are shown in Fig. 4.3.
Normally, the output frequency is restricted due to the Nyquist criteria. This criteria states that the highest frequency signal f_{max} a DAC can generate is equal to half the sampling rate $\frac{f_s}{2}$. This state can be rewritten as

$$f_{max} \leq \frac{f_s}{2}. \tag{4.1}$$

Although this limitation applies to Presto, due to the nature of the output signal generation it is possible to generate signals with frequency above the half the sampling rate. Consider a signal generated at frequency f_0. The real spectrum of the output signal contains this fundamental component. However, additional "spur" components occur in the spectrum as it is indicated in Fig. 4.4. In general, these additional modes are the composition of sampling and generated rate and thus occur at frequencies

$$|C \cdot f_s \pm f_0|, C \in \mathbb{N}. \tag{4.2}$$

Thus, by properly choosing the output frequency and carefully filtering out all the undesired modes one can stimulate the generation of harmonics above the Nyquist limit.
The track of the wire setup, including port correspondence, bandpass filters, attenuation and amplification units, is kept in the Hardware setup Python file. The schematic diagram is depicted in Fig. 4.2 (top) and the example of the hardware setup track in the experiment configuration represented in Listing 4.2.

```
1 SETUP_PRESTO_AMPLIFIER = """
```

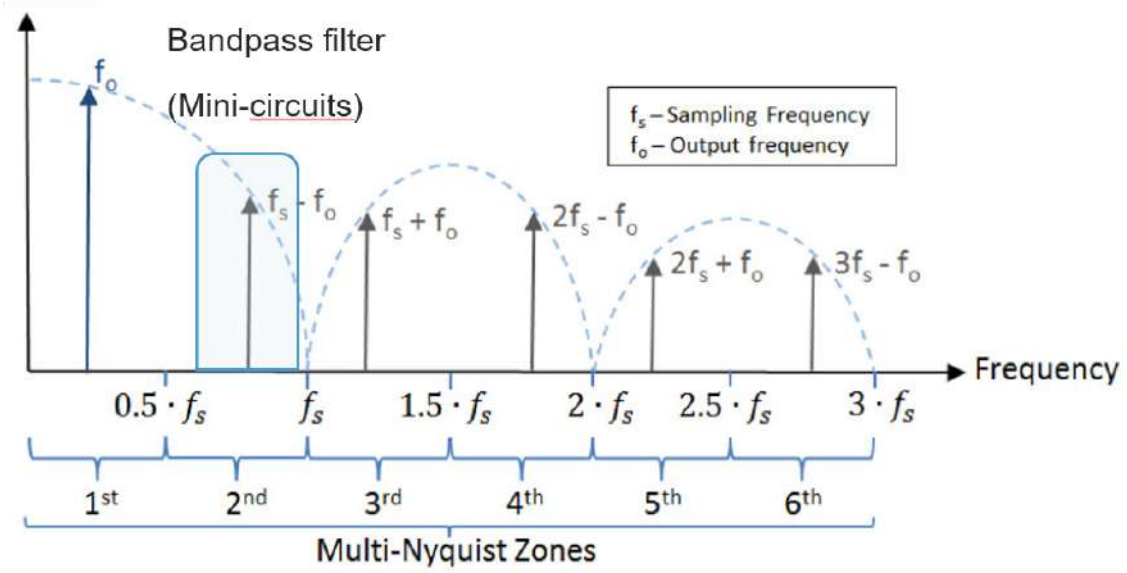

Figure 4.4: The fundamental and "spur" frequencies. A proper bandpass filter allows to filter out all undesired modes.

```
    S3: ((P1 readout drive 1 -> VBFZ-6260-S+ 5.6-7GHz filter ->
2*10 dB atten) \n
    and (P2 readout drive 4 ->  VHP-26 3-7 GHz filter-> \n
    10 dB atten) into MiniCircuits ZFSC-2-10G+ splitter), \n

    N8 (P8 qubit drive 1 -> VBFZ-3590-S+ 3.0-4.3 GHz filter ->
(6*0+10)dB atten -> 12dB ADM1-0026PA amplifier) and \n
        (P5 cavity 1 -> VBFZ-3590-S+ 3-4.3 GHz filter -> 6dB atten
-> 26 dB ZVA-183-S+ amplifier) -> 3 dB atten\n
        into splitter \n

    S4 (P4 qubit drive 4 -> VLF-8400+ DC-8.4 GHz filter -> 0dB
atten -> ZX60-14012L-S+ 12dB amplifier) and \n
        (P7 cavity drive 4 -> VBFZ-6260-S+ 5.6-7.0 GHz filter -> 12
dB ADM1-0026PA amplifier) into splitter, \n

    A4: no attenuation (output line), \n

    N4: P6 coupler charge drive -> VBF-4440+ 4.2-4.7 GHz filter \n

    K1: FL PBC P3 3w-if -> VLFX-2500+ 10-2500 MHz filter -> VXHF
-392+ 3.94-11.5 GHz filter -> 12dB ADM1-0026PA amplifier \n
"""
```

Listing 4.2: Presto wire setup

After the characterization, once all the main parameters are measured and the setup is calibrated, the main experiment can be carried out. Full list of characterized values is given in Appendix.

4.3 Beamsplitting experiment

In this section, the implementation and performance of beamsplitting interaction between two cavities with the readout system is demonstrated by flux driving. The experiment scheme is shown in Fig. 4.5. The realization is as follows: first, one of the cavities is populated with a coherent state via application of displacement operator $D(\alpha)$. This is done by execution of an AC-pulse with resonant frequency on the cavity 1. The relation between the pulse amplitude and the corresponding displacement α is done via calibration. Then, a pulse is applied via flux drive to the coupler with frequency difference between the two cavities which should undergo beamsplitter interaction. This pulse sequence leads to the parametric coupling, described in sec. Theory. The system is consequently read out by performing Wigner tomography on cavity 4. From this point onward, the cavity to which the displacement is applied will be referred to as the "state preparation cavity" (cavity 1), and the cavity undergoing Wigner tomography will be referred to as the "tomography cavity" (cavity 4). In order to acquire information about the complete quantum state, it is essential to perform tomography on all the cavities involved in the experiment. However, in this particular experiment, performing tomography on a single cavity is adequate to demonstrate evidence of the beamsplitting. The Wigner tomography protocol is discussed in the following subsection.

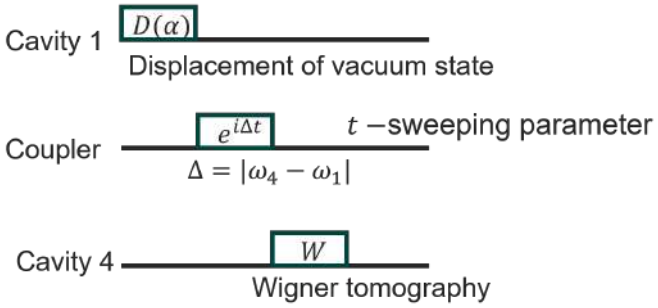

Figure 4.5: Beamsplitting experiment pulse sequence.

4.3.1 Wigner tomography protocol

The schematic representation of the Wigner tomography was shown in, for instance, [46] and is illustrated in Fig. 4.6 (top).
First, the cavity state is displaced by an arbitrary value of α. This action is equivalent to the unitary transformation of the state density matrix with the displacement operator $D^\dagger(\alpha)\rho D(\alpha) = D(-\alpha)\rho D(\alpha)$. Once it is done, an unselective $\frac{\pi}{2}$-pulse is applied to the qubit leading to the superposition state $\frac{|0\rangle+|1\rangle}{2}$ (Fig. 4.6, bottom, step 1 and 2).
Within free evolution the system state, which initially was a tensor product of coherent cavity state and the qubit superposition pure state, becomes entangled and can no longer be factored into two separate subsystem states. After this evolution, the resulting state is

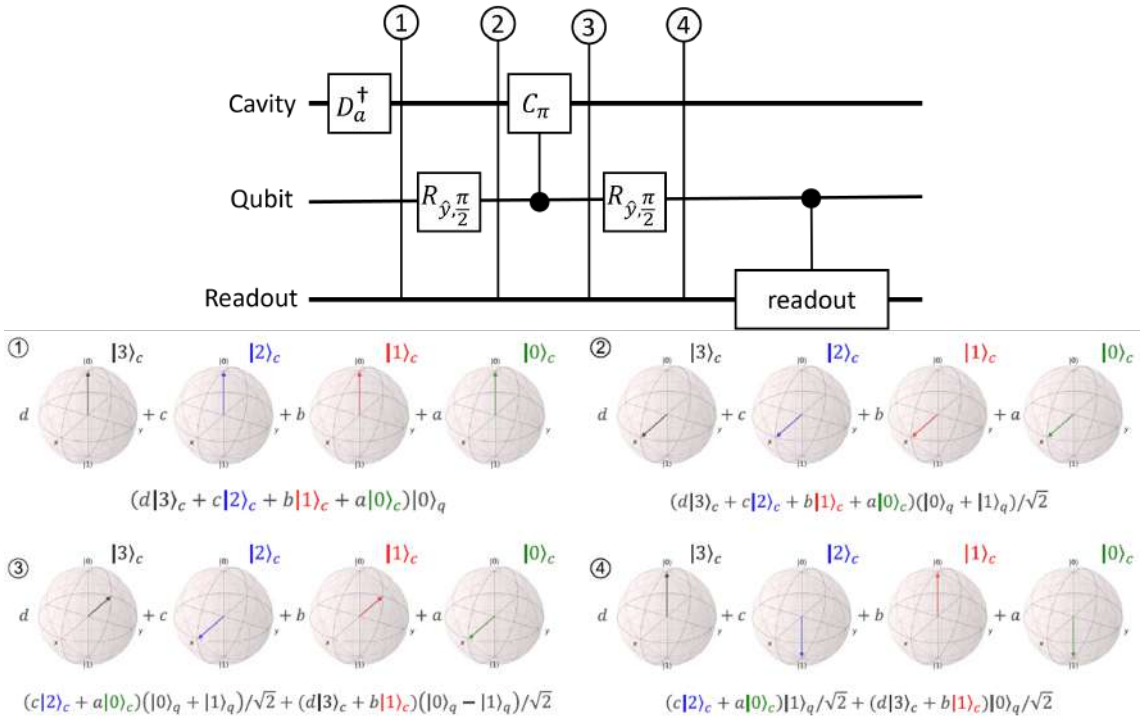

Figure 4.6: Wigner tomography pulse sequence (top) and stepwise transformation of the cavity state (bottom).

$$\hat{U}\,|\psi\rangle = \sum_n C_n \left[|n,0\rangle + e^{2in\chi t}\,|n,1\rangle\right]. \tag{4.3}$$

For $t = \frac{\pi}{2\chi}$ the state transforms into

$$|\psi'\rangle = \sum_n C_n \left[|n,0\rangle + (-1)^n\,|n,1\rangle\right]. \tag{4.4}$$

Thus, according to the eq. 4.4, after free evolution for time $t = \frac{\pi}{2\chi}$ the system state occurs in a summarized superposition of $|+\rangle = \frac{|0\rangle+|1\rangle}{2}$ and $|-\rangle = \frac{|0\rangle-|1\rangle}{2}$, the sign depends on the cavity Fock state. This can be seen as a rotation of the qubit state with frequency proportional to the Fock state number (Fig. 4.6, bottom, step 3). Hence, after applying the second unselective $\frac{\pi}{2}$-pulse on the system state it ends up in

$$|\psi\rangle = \sum_{n_{even}} C_n\,|n,0\rangle + \sum_{n_{odd}} C_n\,|n,1\rangle\,, \tag{4.5}$$

the result for each qubit state in correspondence with the Fock state can be seen in 4.6 (bottom, step 4).
Reading the resulting qubit state after this operation leads to $|0\rangle$ state if the cavity Fock state was even and to $|1\rangle$ state if odd. The corresponding eigenvalues are 1 for $|0\rangle$ and -1 for $|1\rangle$. Thus, by measuring the qubit state we perform the parity measurement of the cavity state, which leads to the conclusion that the performed operation produced the Wigner tomography protocol. By iteratively repeating the

protocol for all values of displacement α within the chosen range and resolution, one generates a map of cavity state parity. This map represents the quasiprobability distribution of the cavity quantum state, which uniquely characterizes the bosonic state. Negative values of Wigner function in tomography would indicate a non-classical state.

Establishing the correspondence between the color map obtained through tomography and the initial bosonic state is not straightforward, this task requires complex analysis and calculation. In this research, the beamsplitting is observed between the cavities with one of them initially populated with a coherent state. The Wigner function of a coherent state is well-known and can be easily identified and fitted.

4.3.2 Beamsplitting via flux drive

To setup the following experiment, a separate class "CavityBeamsplittingViaFlux" for Presto script was created. The full code can be found in Appendix. The designed experiment inherits "StateTomography" class, which produces the Wigner Tomography for the chosen cavity. This parent class takes configurations and a pulse sequence, which are defined in the child class "CavityBeamsplittingViaFlux". The child class in turn contains two methods. The first, "set_up_state_preparation", sets up look-up tables, mixers and local oscillator frequencies for the state preparation cavity and for the flux drive. Second, "state_preparation_pulse_sequence" takes the configuration defined in previous method, pulse definitions and other necessary primary parameters. It subsequently arranges the sequence of pulses according to the prime parameters established beforehand.

The "get_cavity_beamsplitting_via_flux_config" function allows to define the primary parameters of the setup and create IQ-mixers for the target state cavity and for the coupler. This function is then called in the main measurement sequence, in which the user defines the branch order, bias voltage for the external flux, displacement for coherent state α and flux pulse shape.
Taking $\alpha = 1.9$ as the displacement for coherent state in the state preparation cavity, the experiment is performed at coupler's Kerr-free point. Within the experiment, the flux pulse duration varies from 0 to 2000 ns. After the flux pulse a Wigner tomography is performed on the tomography branch cavity.
The resulting tomography images taken at different time stamps can be seen in Fig. 4.7. Here, at $t = 10$ ns the Wigner function reads out the vacuum state since no flux pulse yet applied. With the pulse duration increasing, one can visually evaluate the transition of the "blob" in the phase space.

To characterize the generated data, the overlap between each obtained tomography picture and fitted coherent state is calculated, the corresponding results can be seen in Fig. 4.8. This Figure represents the dynamics of fitted α in dependency on increasing flux pulse duration. The behaviour is qualitatively similar to the example observed in Fig. 2.1b. One can notice that the state gradually fades away; this is due to decoherence effects, as the cavities' lifetimes are short

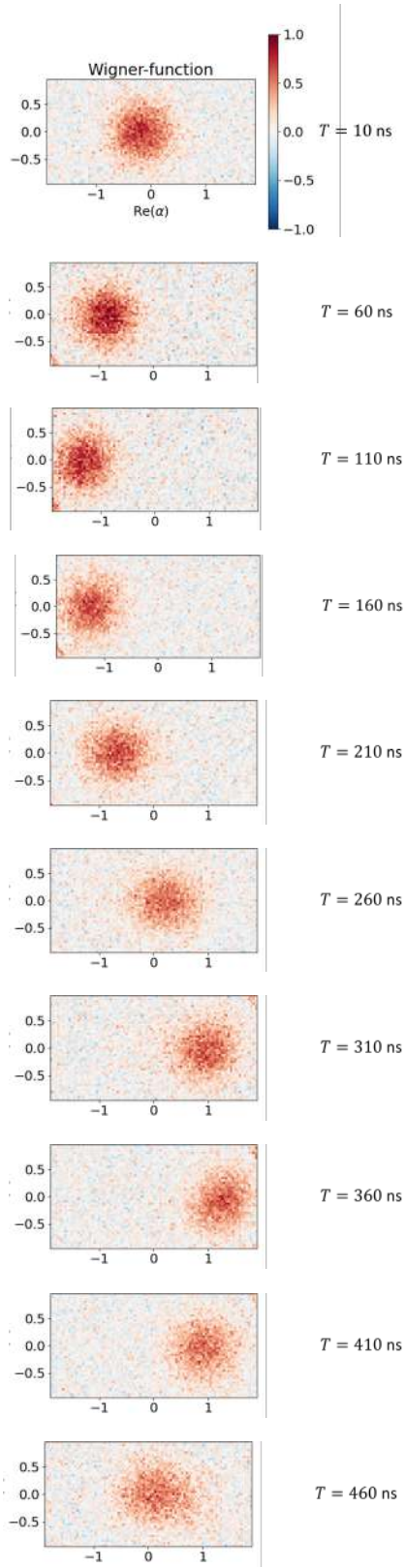

Figure 4.7: The tomography images of branch 4 cavity obtained at various times of pulse duration stamps for beamsplitting via flux drive experiment. Pulse duration varies from 10 to 260 ns.

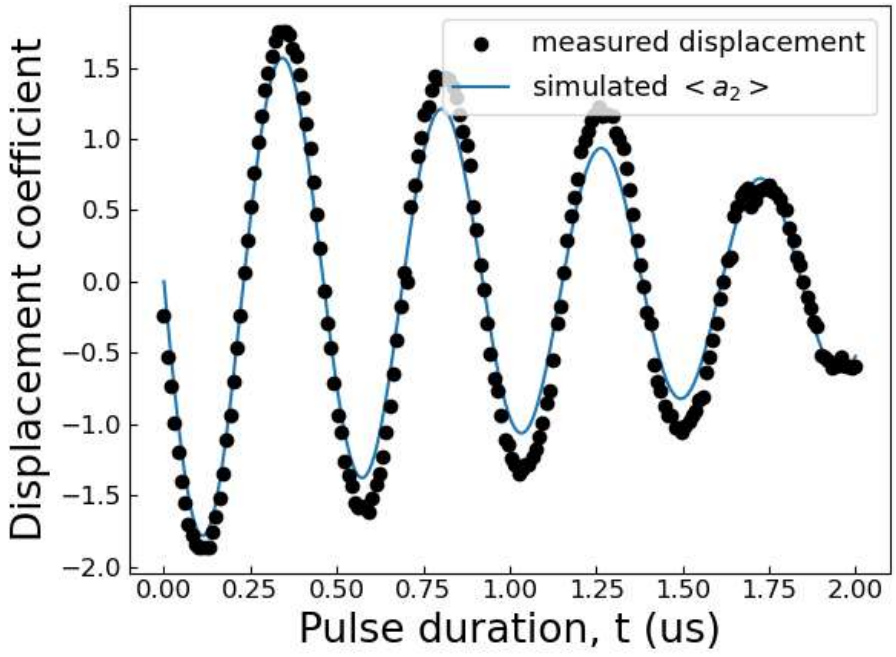

Figure 4.8: Fitted with experimental data from Wigner tomography displacement α.

To validate the behavior of the measured displacement, a simulation of the beamsplitting interaction was performed. The QuTiP library for Python was utilized to simulate the Lindblad master equation. For the Hamiltonian part, the interaction given in Equation 2.12 was used, while the jump operators were taken in the following forms

$$\begin{aligned} D_1 &= \sqrt{\kappa_{a1}} \cdot a_1^\dagger a_1, \\ D_2 &= \sqrt{\frac{1}{T_1^{a1}}} \cdot a_1, \\ D_3 &= \sqrt{\kappa_{a2}} \cdot a_2^\dagger a_2, \\ D_4 &= \sqrt{\frac{1}{T_1^{a2}}} \cdot a_2, \end{aligned} \tag{4.6}$$

Here, T_1^{a1}, T_2^{a1} are relaxation and dephasing times of the first mode, and T_1^{a2}, T_2^{a2} – of the second mode. κ_{a1}, κ_{a2} are pure dephasing rates calculated as

$$\begin{aligned} \kappa_{a1} &= \frac{1}{T_2^{a1}} - \frac{1}{2T_1^{a1}}, \\ \kappa_{a2} &= \frac{1}{T_2^{a2}} - \frac{1}{2T_1^{a2}}. \end{aligned} \tag{4.7}$$

The values of decoherence times are determined through the characterization of the chip, while the coupling rate of the beamsplitting interaction was extracted from the experiment.

5
Conclusion

Within the work on this project, we investigated strategies for coupling bosonic modes. A novel planar bosonic platform was designed featuring the simultaneous implementation of four cavities interconnected by a single coupler. This prospect gives an insight on potential further bosonic modes scaling. Parameters of the design were consequently verified by carried out characterization. The introduced coupler was realized as a nonlinear circuit incorporating a SNAIL element. This innovative structure facilitates mode interaction while cancelling the impact of undesired nonlinear effects. Two distinct beamsplitting mechanisms were proposed, each involving the utilization of second- and third-order terms of the system's Hamiltonian. For one out of two proposed mechanisms for beamsplitting interaction the experiment has shown expected result, the beamsplitting via 3WM remains for future investigation.

Implementation of precise hardware setup like Presto allowed to carefully control pulse sequence and perform the experiment on achieving beamsplitting interaction via flux drive. Evidence of coherent state initialization within a state preparation cavity and its subsequent transfer to a tomography cavity through parametric coupling was effectively demonstrated using Wigner tomography.

The characterization of the first chip design provided essential understanding into planar chip design, including aspects such as coupling strength to the transmission line and the geometry of air bridges. These insights will be taken into account for the next chip generation. In the next step, it is intriguing to implement independent and simultaneous beamsplitting for multiple pairs of cavities. The approach for intercavity interaction via a SNAIL element potentially opens a path toward new two-mode gate mechanisms.

Bibliography

[1] Shor, Peter W. "Algorithms for quantum computation: discrete logarithms and factoring." *Proceedings 35th annual symposium on foundations of computer science*. Ieee, 1994.

[2] Grover, L. K. (1997). Quantum mechanics helps in searching for a needle in a haystack. *Physical review letters*, 79(2), 325.

[3] Deutsch, D., Jozsa, R. (1992). Rapid solution of problems by quantum computation. *Proceedings of the Royal Society of London. Series A: Mathematical and Physical Sciences*, 439(1907), 553-558.

[4] Gambetta, J. M., Chow, J. M., Steffen, M. (2017). Building logical qubits in a superconducting quantum computing system. npj quantum information, 3(1), 2.

[5] Gong, M., Wang, S., Zha, C., Chen, M. C., Huang, H. L., Wu, Y., ... Pan, J. W. (2021). Quantum walks on a programmable two-dimensional 62-qubit superconducting processor. Science, 372(6545), 948-952.

[6] Lloyd, S., Braunstein, S. L. (1999). Quantum computation over continuous variables. *Physical Review Letters*, 82(8), 1784.

[7] Yokoyama, S., Ukai, R., Armstrong, S. C., Sornphiphatphong, C., Kaji, T., Suzuki, S., ... Furusawa, A. (2013). Ultra-large-scale continuous-variable cluster states multiplexed in the time domain. *Nature Photonics*, 7(12), 982-986.

[8] Gottesman, D., Kitaev, A., Preskill, J. (2001). Encoding a qubit in an oscillator. *Physical Review A*, 64(1), 012310.

[9] Baragiola, B. Q., Pantaleoni, G., Alexander, R. N., Karanjai, A., Menicucci, N. C. (2019). All-Gaussian universality and fault tolerance with the Gottesman-Kitaev-Preskill code. *Physical review letters*, 123(20), 200502.

[10] Cai, W., Ma, Y., Wang, W., Zou, C. L., Sun, L. (2021). Bosonic quantum error correction codes in superconducting quantum circuits. *Fundamental Research*, 1(1), 50-67.

[11] Paik, H., Schuster, D. I., Bishop, L. S., Kirchmair, G., Catelani, G., Sears, A. P., ... Schoelkopf, R. J. (2011). Observation of high coherence in Josephson junction qubits measured in a three-dimensional circuit QED architecture. *Physical Review Letters*, 107(24), 240501.

[12] Reagor, M., Pfaff, W., Axline, C., Heeres, R. W., Ofek, N., Sliwa, K., ... Schoelkopf, R. J. (2016). Quantum memory with millisecond coherence in circuit QED. *Physical Review B*, 94(1), 014506.

[13] Axline, C., Reagor, M., Heeres, R., Reinhold, P., Wang, C., Shain, K., ... Schoelkopf, R. J. (2016). An architecture for integrating planar and 3D cQED devices. *Applied Physics Letters*, 109(4).

[14] Kudra, M. (2022). *Building a Bosonic Microwave Qubit*. Chalmers Tekniska Hogskola (Sweden).

[15] Eichler, C. (2013). *Experimental characterization of quantum microwave radiation and its entanglement with a superconducting qubit* (Doctoral dissertation, ETH Zurich).

[16] Krantz, P., Kjaergaard, M., Yan, F., Orlando, T. P., Gustavsson, S., Oliver, W. D. (2019). A quantum engineer's guide to superconducting qubits. *Applied physics reviews*, 6(2).

[17] Koch, J., Terri, M. Y., Gambetta, J., Houck, A. A., Schuster, D. I., Majer, J., ... Schoelkopf, R. J. (2007). Charge-insensitive qubit design derived from the Cooper pair box. Physical Review A, 76(4), 042319.

[18] Boyd, R. W., Gaeta, A. L., Giese, E. (2008). Nonlinear optics. In *Springer Handbook of Atomic, Molecular, and Optical Physics* (pp. 1097-1110). Cham: Springer International Publishing.

[19] Baust, A., Hoffmann, E., Haeberlein, M., Schwarz, M. J., Eder, P., Goetz, J., ... Gross, R. (2015). Tunable and switchable coupling between two superconducting resonators. *Physical Review B*, 91(1), 014515.

[20] Hoi, I. C., Kockum, A. F., Palomaki, T., Stace, T. M., Fan, B., Tornberg, L., ... Wilson, C. M. (2013). Giant cross–Kerr effect for propagating microwaves induced by an artificial atom. *Physical review letters*, 111(5), 053601.

[21] Allman, M. S., Whittaker, J. D., Castellanos-Beltran, M., Cicak, K., da Silva, F., DeFeo, M. P., ... Simmonds, R. W. (2014). Tunable resonant and nonresonant interactions between a phase qubit and L C resonator. *Physical review letters*, 112(12), 123601.

[22] Pierre, M., Svensson, I. M., Raman Sathyamoorthy, S., Johansson, G., Delsing, P. (2014). Storage and on-demand release of microwaves using superconducting resonators with tunable coupling. *Applied Physics Letters*, 104(23).

[23] Flurin, E., Roch, N., Pillet, J. D., Mallet, F., Huard, B. (2015). Superconducting quantum node for entanglement and storage of microwave radiation. *Physical review letters*, 114(9), 090503.

[24] Sirois, A. J., Castellanos-Beltran, M. A., DeFeo, M. P., Ranzani, L., Lecocq, F., Simmonds, R. W., ... Aumentado, J. (2015). Coherent-state storage and retrieval between superconducting cavities using parametric frequency conversion. *Applied Physics Letters*, 106(17).

[25] Yin, Y., Chen, Y., Sank, D., O'Malley, P. J. J., White, T. C., Barends, R., ... Martinis, J. M. (2013). Catch and release of microwave photon states. *Physical review letters*, 110(10), 107001.

[26] Peropadre, B., Zueco, D., Wulschner, F., Deppe, F., Marx, A., Gross, R., García-Ripoll, J. J. (2013). Tunable coupling engineering between superconducting resonators: From sidebands to effective gauge fields. *Physical Review B*, 87(13), 134504.

[27] Gao, Y. Y., Lester, B. J., Zhang, Y., Wang, C., Rosenblum, S., Frunzio, L., ... Schoelkopf, R. J. (2018). Programmable interference between two microwave quantum memories. *Physical Review X*, 8(2), 021073.

[28] Leghtas, Z., Touzard, S., Pop, I. M., Kou, A., Vlastakis, B., Petrenko, A., ... Devoret, M. H. (2015). Confining the state of light to a quantum manifold by engineered two-photon loss. *Science*, 347(6224), 853-857.

[29] Frattini, N. E., Vool, U., Shankar, S., Narla, A., Sliwa, K. M., Devoret, M. H. (2017). 3-wave mixing Josephson dipole element. *Applied Physics Letters*, 110(22).

[30] Sivak, V. V., Frattini, N. E., Joshi, V. R., Lingenfelter, A., Shankar, S., Devoret, M. H. (2019). Kerr-free three-wave mixing in superconducting quantum circuits. *Physical Review Applied*, 11(5), 054060.

[31] Ranadive, A., Esposito, M., Planat, L., Bonet, E., Naud, C., Buisson, O., ... Roch, N. (2021). A reversed Kerr traveling wave parametric amplifier. arXiv e-prints, arXiv-2101.

[32] Fadavi Roudsari, A., Shiri, D., Renberg Nilsson, H., Tancredi, G., Osman, A., Svensson, I. M., ... Delsing, P. (2023). Three-wave mixing traveling-wave parametric amplifier with periodic variation of the circuit parameters. *Applied Physics Letters*, 122(5).

[33] Mari, A., Eisert, J. (2012). Positive Wigner functions render classical simulation of quantum computation efficient. *Physical review letters*, 109(23), 230503.

[34] Lu, Y., Maiti, A., Garmon, J. W., Ganjam, S., Zhang, Y., Claes, J., ... Schoelkopf, R. J. (2023). A high-fidelity microwave beamsplitter with a parity-protected converter. *arXiv preprint* arXiv:2303.00959.

[35] Broome, M. A., Fedrizzi, A., Rahimi-Keshari, S., Dove, J., Aaronson, S., Ralph, T. C., White, A. G. (2013). Photonic boson sampling in a tunable circuit. *Science*, 339(6121), 794-798.

[36] Scheel, S. (2004). Permanents in linear optical networks. arXiv preprint quant-ph/0406127.

[37] Waldram, J. R. (2017). Superconductivity of metals and cuprates. CRC Press.

[38] Wang, X. (2001). Continuous-variable and hybrid quantum gates. *Journal of Physics A: Mathematical and General*, 34(44), 9577.

[39] Chapman, B. J., de Graaf, S. J., Xue, S. H., Zhang, Y., Teoh, J., Curtis, J. C., ... Schoelkopf, R. J. (2022). A high on-off ratio beamsplitter interaction for gates on bosonically encoded qubits. *arXiv preprint* arXiv:2212.11929.

[40] Veitch, V., Ferrie, C., Gross, D., Emerson, J. (2012). Negative quasi-probability as a resource for quantum computation. New Journal of Physics, 14(11), 113011.

[41] Eickbusch, A., Sivak, V., Ding, A. Z., Elder, S. S., Jha, S. R., Venkatraman, J., ... Devoret, M. H. (2022). Fast universal control of an oscillator with weak dispersive coupling to a qubit. Nature Physics, 18(12), 1464-1469.

[42] Gerry, C., Knight, P. L. (2005). Introductory quantum optics. *Cambridge university press*.

[43] Kudra, M., Kervinen, M., Strandberg, I., Ahmed, S., Scigliuzzo, M., Osman, A., ... Gasparinetti, S. (2022). Robust preparation of Wigner-negative states with optimized SNAP-displacement sequences. *PRX Quantum*, 3(3), 030301.

[44] Moskalev, D. O., Zikiy, E. V., Pishchimova, A. A., Ezenkova, D. A., Smirnov, N. S., Ivanov, A. I., ... Rodionov, I. A. (2023). Optimization of shadow evaporation and oxidation for reproducible quantum Josephson junction circuits. *Scientific Reports*, 13(1), 4174.

[45] Tholén, M. O., Borgani, R., Di Carlo, G. R., Bengtsson, A., Križan, C., Kudra, M., ... Haviland, D. B. (2022). Measurement and control of a superconducting quantum processor with a fully integrated radio-frequency system on a chip. *Review of Scientific Instruments*, 93(10).

[46] Vlastakis, B., Kirchmair, G., Leghtas, Z., Nigg, S. E., Frunzio, L., Girvin, S. M., ... Schoelkopf, R. J. (2013). Deterministically encoding quantum information using 100-photon Schrödinger cat states. *Science*, 342(6158), 607-610.

[47] Clarke, J., Braginski, A. I. (2004). The SQUID handbook (Vol. 1, pp. 277-280). Weinheim: Wiley-Vch.

[48] Manucharyan, V. E., Koch, J., Glazman, L. I., Devoret, M. H. (2009). Fluxonium: Single cooper-pair circuit free of charge offsets. *Science*, 326(5949), 113-116.

[49] Grimm, A., Frattini, N. E., Puri, S., Mundhada, S. O., Touzard, S., Mirrahimi, M., ... Devoret, M. H. (2020). Stabilization and operation of a Kerr-cat qubit. *Nature*, 584(7820), 205-209.

[50] github.com/202Q-lab/OQTO

[51] Minev, Z. K., Leghtas, Z., Mundhada, S. O., Christakis, L., Pop, I. M., Devoret, M. H. (2021). Energy-participation quantization of Josephson circuits. npj Quantum Information, 7(1), 131.

A

Appendix

A.1 Source code listing

A.1.1 CavityBeamsplitingViaFlux class

```
class CavityBeamsplitingViaFlux(StateTomography):
    """
    Experiment class for preparing a cavity state, transferring it to another cavity via a flux pulse to a coupler,
    and then measuring the state in the second cavity by Wigner tomography.
    """
    def set_up_state_preparation(self, pls):
        pp = self.config['primary_parameters']
        pulse_defs = self.config['pulse_definitions']
        mixers = self.config['mixers']
        # set up displacement cavity pulse LUT
        self.setup_default_luts(pls, 'state_prep_disp_pulse_x', offset_angle=0)
        # set up mixers and tomography
        cavity_lo = pp['state_prep_cavity_freq'] + pulse_defs['state_prep_disp_pulse_x']['intermediate_frequency']
        self.configure_mixer(pls, 'state_prep_cavity', cavity_lo)
        # set up flux pulse LUT
        self.setup_default_luts(pls, 'coupler_pulse', offset_angle=pp['coupler_pulse_angle'])
        # set up mixers and tomography
        flux_lo = pp['pulse_frequency'] + pulse_defs['coupler_pulse']['intermediate_frequency']
        self.configure_mixer(pls, pp['coupler_mixer_name'], flux_lo)
    def state_preparation_pulse_sequence(self, pls, time):
        pulse_defs = self.config['pulse_definitions']
        mixers = self.config['mixers']
        pp = self.config['primary_parameters']
        # Send pulses
        disp_pulse = self.pulses['state_prep_disp_pulse_x']
        disp_length = pulse_defs['state_prep_disp_pulse_x']['length']
        pls.reset_phase(time, mixers['state_prep_cavity']['out_port'])
        pls.select_scale(time, 0, [mixers['state_prep_cavity']['out_port']], group=pulse_defs['state_prep_disp_pulse_x']['group'])
```

```
        pls.output_pulse(time, [disp_pulse])
        time += disp_length
        coupler_pulse = self.pulses['coupler_pulse']
        coupler_length = pulse_defs['coupler_pulse']['length']
        pls.reset_phase(time, mixers[pp['coupler_mixer_name']]['out_port'])
        pls.select_scale(time, 0, [mixers[pp['coupler_mixer_name']]['out_port']], group=pulse_defs['coupler_pulse']['group'])
        pls.output_pulse(time, [coupler_pulse])
        time += coupler_length
        return time
```

A.1.2 Configuration of primary parameters for the experiment

```
def get_cavity_beamsplitting_via_flux_config(
    cfg_state_prep_branch: dict,
    cfg_tomography_branch: dict,
    coupler_pulses: list,
    instruments: dict,
    state_preparation_disp_alpha: float,
    coupler_pulse_amp: float,
    coupler_pulse_length: float,
    coupler_pulse_angle: float,
):
    config = get_cavity_wigner_tomography_base_config(cfg_tomography_branch, instruments)
    config["name"] = "cavity_beamsplitting_via_flux"
    config["primary_parameters"]["state_prep_cavity_freq"] = cfg_state_prep_branch[ac.CAVITY_FREQ]
    config["primary_parameters"]["state_preparation_disp_alpha"] = state_preparation_disp_alpha
    config["primary_parameters"]["pulse_frequency"] = abs(cfg_tomography_branch[ac.CAVITY_FREQ] - cfg_state_prep_branch[ac.CAVITY_FREQ])
    config["primary_parameters"]["cavity_freq_state_prep_branch"] = cfg_state_prep_branch[ac.CAVITY_FREQ]
    config["primary_parameters"]["coupler_pulse_amp"] = coupler_pulse_amp
    config["primary_parameters"]["coupler_pulse_length"] = coupler_pulse_length
    config["primary_parameters"]["coupler_pulse_angle"] = coupler_pulse_angle
    coupler_mixer_name = coupler_pulses['mixer']
    config["primary_parameters"]["coupler_mixer_name"] = coupler_mixer_name
    mixer_name_state_prep = "state_prep_cavity"
    config["pulse_definitions"]["state_prep_disp_pulse_x"] = deepcopy(cfg_state_prep_branch[ac.PULSES][ac.CAVITY_DISPLACEMENT_PULSE])
    config["pulse_definitions"]["state_prep_disp_pulse_x"]['mixer'] = mixer_name_state_prep
    config["pulse_definitions"]["state_prep_disp_pulse_x"]['amplitude'] = state_preparation_disp_alpha/cfg_state_prep_branch
```

```
    [ac.CAVITY_DISP_AMP_TO_ALPHA]
26      config["pulse_definitions"]["coupler_pulse"] = deepcopy(
    coupler_pulses)
27      config["pulse_definitions"]["coupler_pulse"]['amplitude'] =
    coupler_pulse_amp
28      config["pulse_definitions"]["coupler_pulse"]['
    coupler_pulse_angle'] = coupler_pulse_angle
29      config["pulse_definitions"]["coupler_pulse"]['length'] =
    coupler_pulse_length
30      config["mixers"][coupler_mixer_name] = cfg_tomography_branch[ac
    .MIXERS][coupler_mixer_name]
31      config["mixers"][mixer_name_state_prep] = cfg_state_prep_branch
    [ac.MIXERS][ac.CAVITY]
32      return config
```

A.2 Experiment procedures

A.2.1 Frequency domain measurements

A.2.1.1 Onetone spectroscopy

To perform one-tone spectroscopy, a continuous pulse is applied to the resonator, and the signal transmitted over the transmission line is detected (Fig. A.1a). An example of this measurement is illustrated in Fig. A.1b.

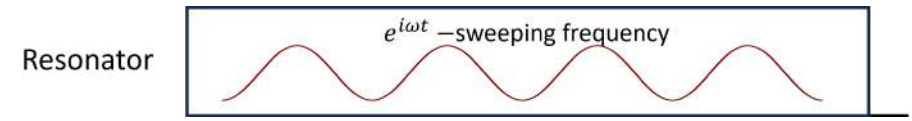

(a)

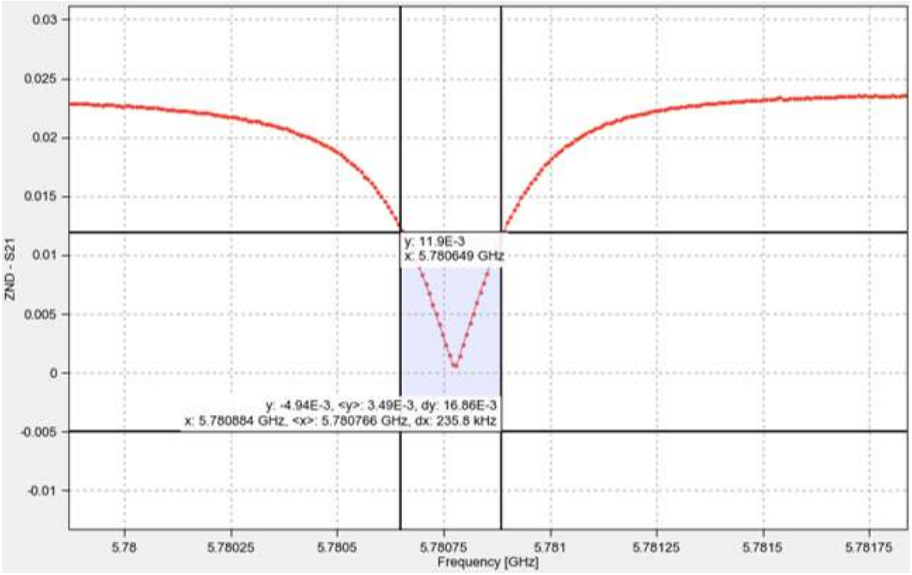

(b)

Figure A.1: a) pulse sequence for onetone S_{21} measurement b) Result of this measurement for resonator 1.

A.2.1.2 Twotone spectroscopy

Subsequently, two-tone spectroscopy is performed by applying a continuous pulse with swept frequency to the qubit. The resulting response is measured via readout at the resonator's resonant frequency. As the qubit and resonator are dispersively coupled, the resonant frequency of the resonator is influenced by the population of the transmon qubit. When the swept frequency aligns with the qubit resonance, the qubit population changes, causing the readout to shift out of resonance with the resonator. This shift in the spectrum can be observed (Fig. A.2a).

Because a transmon operates as a nonlinear harmonic oscillator, its energy levels are not evenly spaced. The difference in energy between two consecutive levels is

determined by the qubit's anharmonicity coefficient α (Fig. A.2b). By applying a sufficiently strong qubit pulse to perform higher energy excitations, the anharmonicity can be identified and quantified.

Another noteworthy nonlinear effect that can be observed in the qubit's spectrum is two-photon absorption. When a certain level of qubit pump power is reached, a process involving the absorption of two photons with equal energies occurs instead of the direct $g - f$ excitation. In this process, the first photon excites the qubit to a virtual level, and the next photon subsequently excites the qubit from the virtual level to the f level. This effect, along with both the $g - e$ and $e - f$ transitions, can be observed in the colormap spectrum, as demonstrated in the qubit 4 measurement shown in Fig. A.2c.

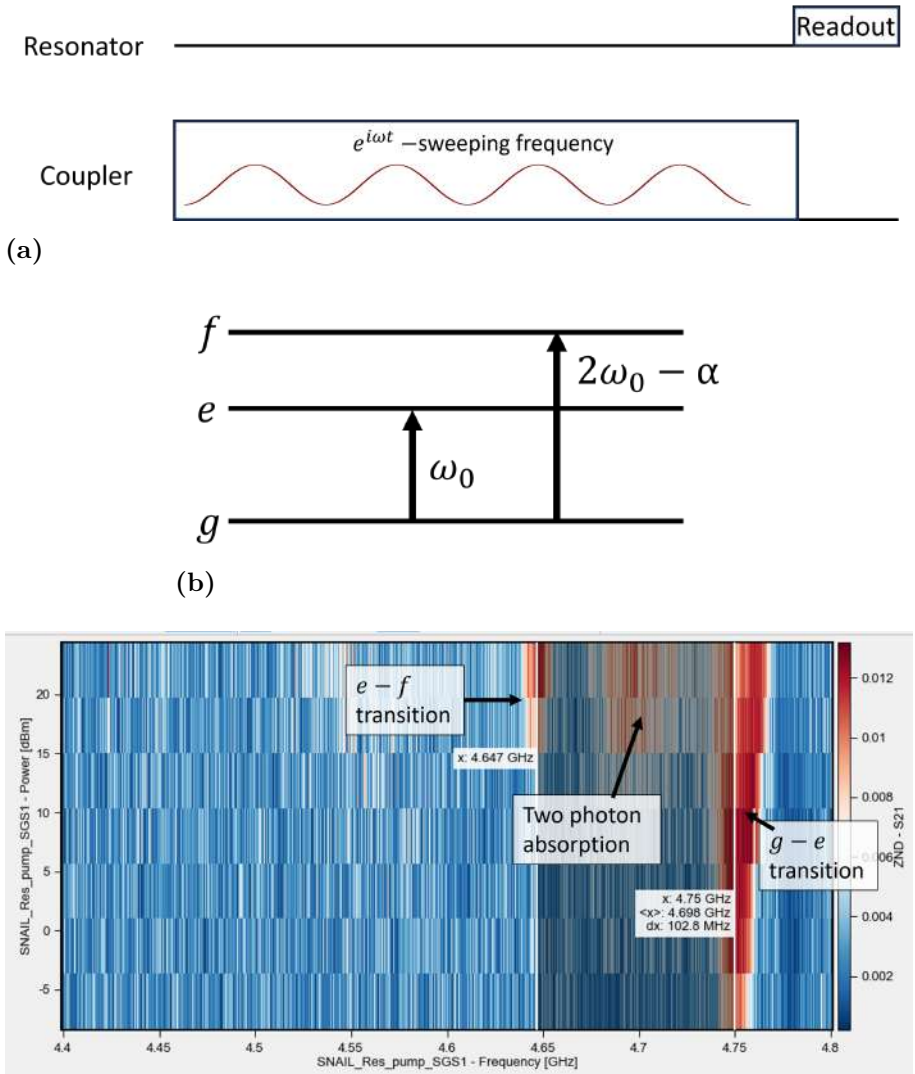

Figure A.2: a) Twotone spectroscopy pulse sequence b) Definition of anharmonicity c) Twotone spectroscopy colormap with respect to the voltage pulse amplitude

A.2.1.3 Onetone of Cavity 2 while sweeping the external flux

In this chip design, cavity 2 can serve as a readout resonator, allowing for onetone spectroscopy. However, due to its coupling to a SNAIL transmon, its eigenfrequency is influenced by the external flux applied to the SNAIL. Therefore, by conducting onetone spectroscopy while simultaneously sweeping the DC voltage on the external flux source (as shown in Fig. A.3a), it becomes possible to observe changes in the colormap representing the cavity frequency as a function of the external flux (Fig. A.3b).

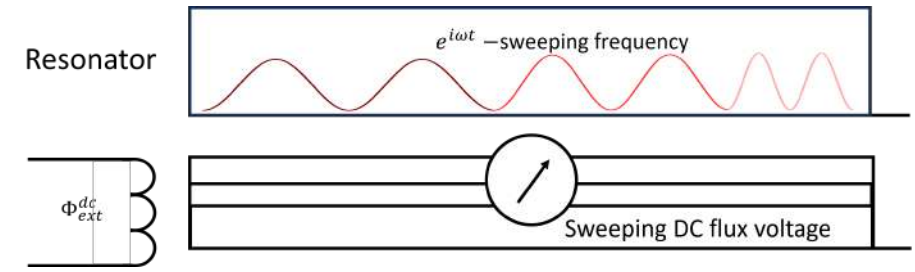

(a)

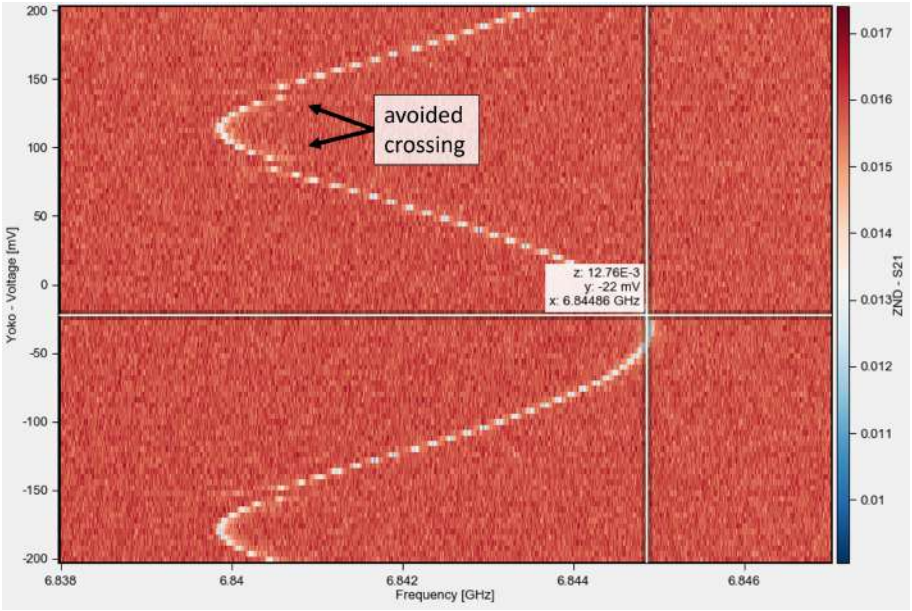

(b)

Figure A.3: a) onetone spectroscopy of cavity 2 with external flux voltage sweep b) spectrum colormap with respect to the external flux voltage amplitude.

A.2.1.4 Coupler resonant frequency with respect to the external flux

Following this, the SNAIL coupler can be treated as a dispersively coupled transmon to cavity 2. Conducting twotone spectroscopy on the coupler allows for the measurement of its eigenfrequency. By iteratively adjusting the amplitude of the flux voltage, it becomes possible to characterize the dependence of the coupler's frequency on the external flux (as shown in Fig. A.4a). The resulting data is illustrated in Fig. A.4b.

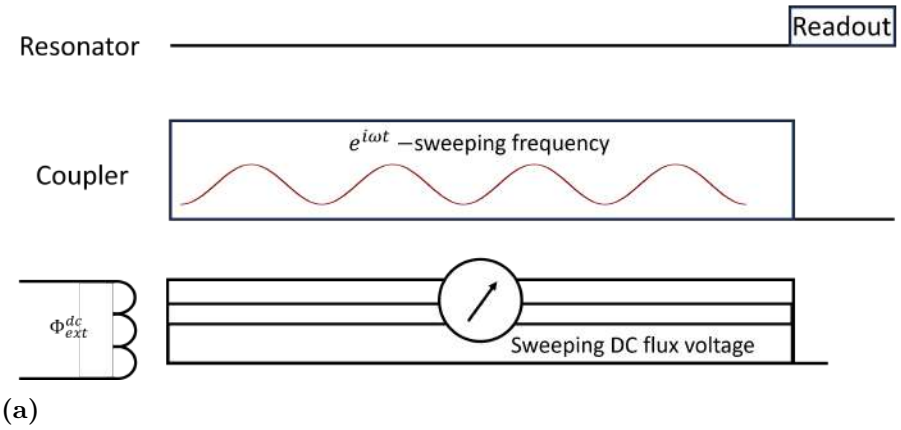

(a)

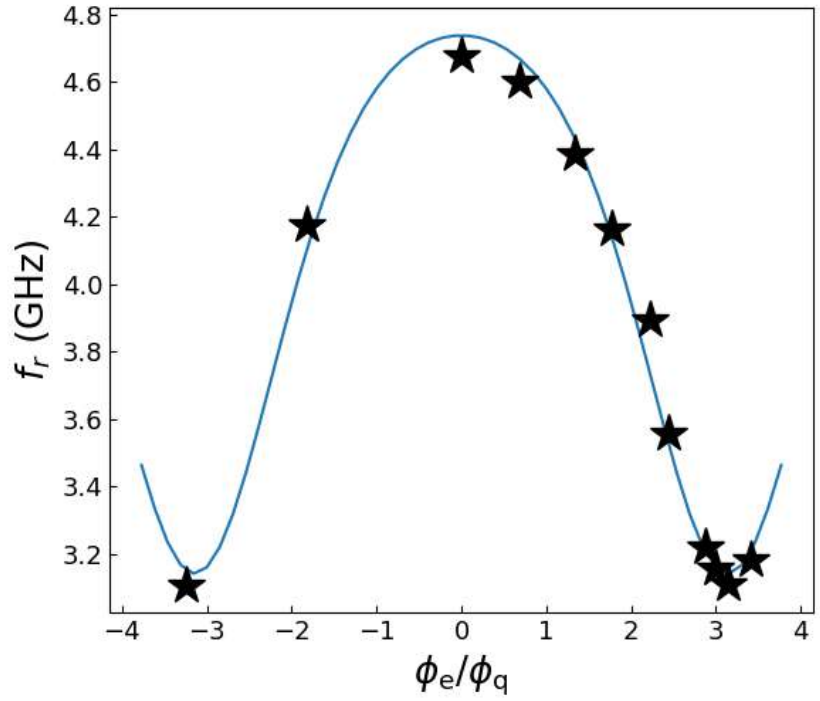

(b)

Figure A.4: a) pulse sequence for performing SNAIL coupler spectrum readout b) The resulting frequency dependency with frequency turning over one flux quanta. The fit for potential w.r.t. flux gives the value of $\alpha = 0.13$.

A.2.2 Time domain measurements

A.2.2.1 One- and twotone spectroscopy

Similar measurements to the one preformed via VNA in A.2.1 can be carried out with Presto. The result for one- and twotoned spectrsocopy is shown in Fig. A.5.

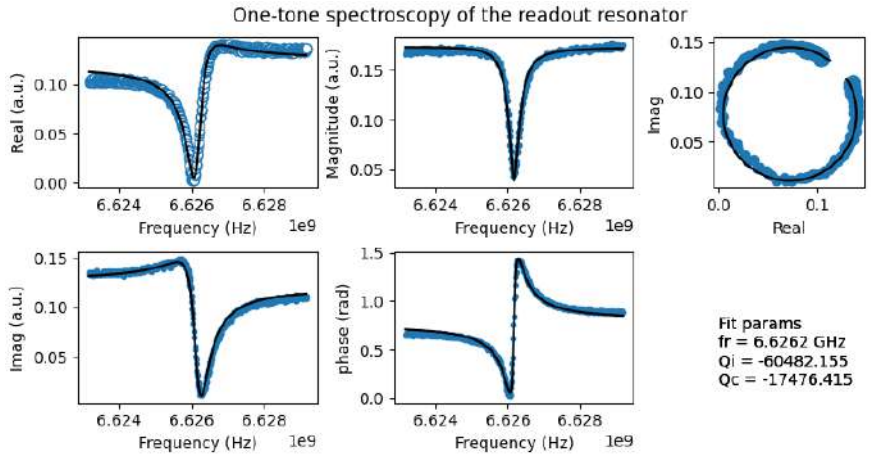

(a)

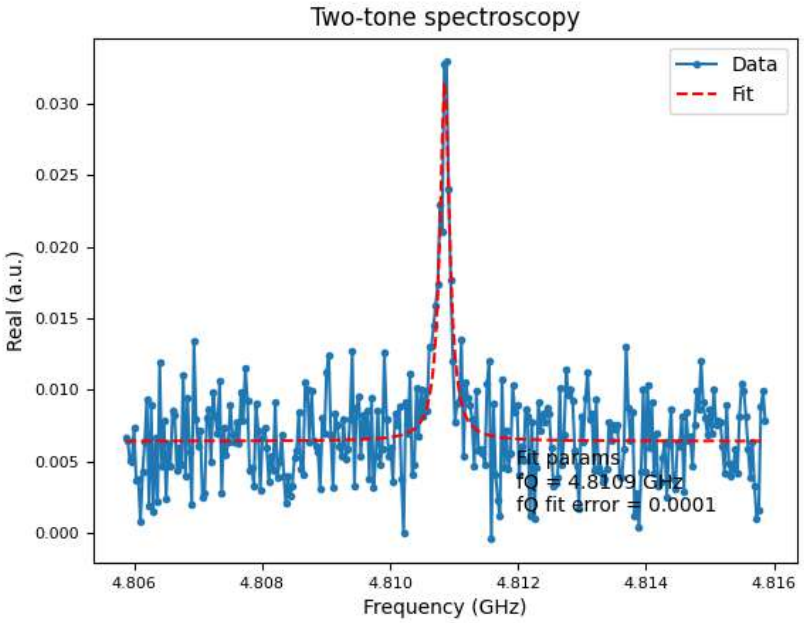

(b)

Figure A.5: a) onetone spectroscopy b) twotone spectroscopy. Both performed with Presto machine.

A.2.2.2 Qubit Rabi oscillation

To find out qubit's π-pulse amplitude, Rabi oscillations were preformed (Fig. A.6a). Resulting measurement is shown in Fig. A.6b.

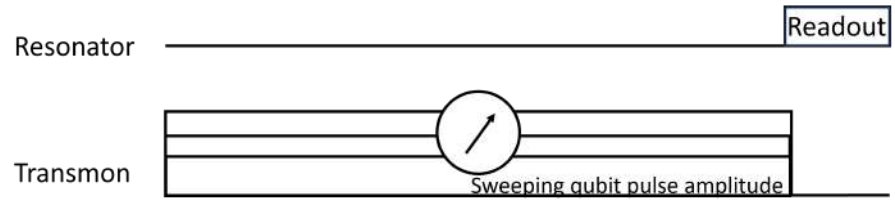

(a)

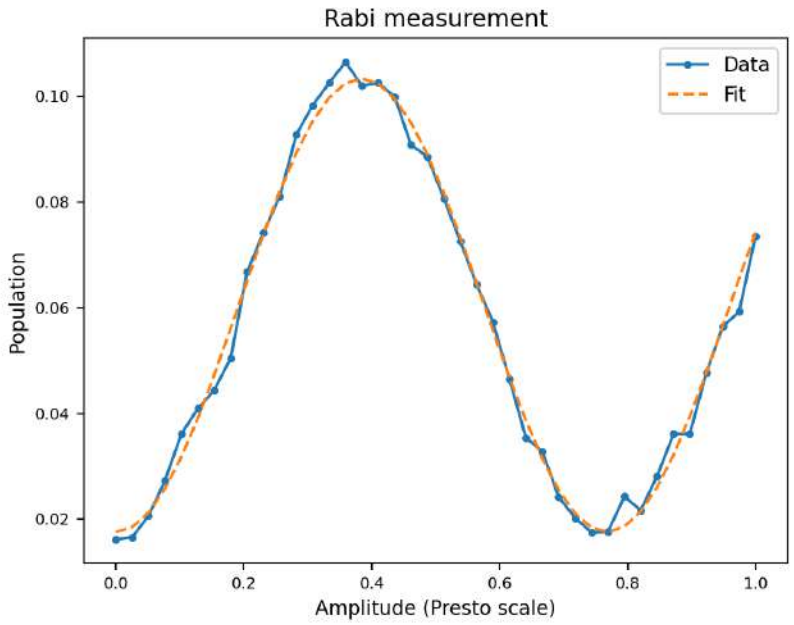

(b)

Figure A.6: a) pulse sequence for Rabi oscillations measurement b) resulting oscillations for qubit 1 population.

A.2.2.3 Qubit selective and unselective Rabi

Due to the dispersive coupling between the transmon and the cavities, the qubit's operational regime becomes sensitive to the cavity's population. By employing a longer-duration pulse, this sensitivity can be taken into account, allowing the excitation to occur within a narrower frequency range (as depicted in Fig. A.7a). In this scenario, a π-pulse only excites the qubit if the cavity is in the Fock state $|0\rangle$. This type of Rabi oscillation is referred to as selective Rabi oscillation, and an illustrative example is shown in Fig. A.8a. On the contrary, a short-duration pulse results in a broader frequency excitation range around the qubit's bare resonant frequency (as shown in Fig. A.7b). The corresponding Rabi oscillations in this case are termed unselective Rabi oscillations, and can be observed in Fig. A.8b.

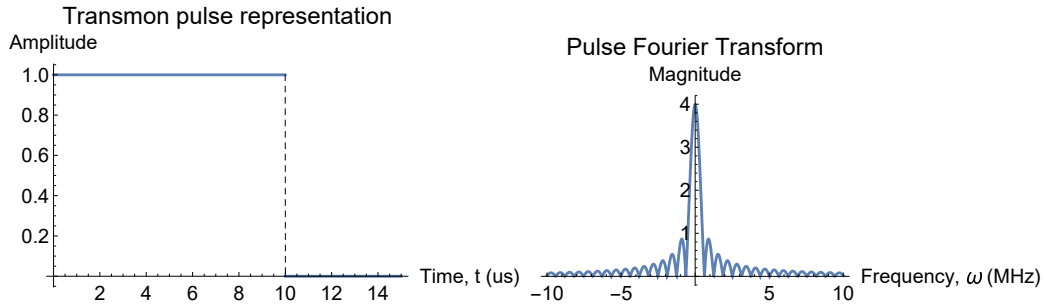

(a)

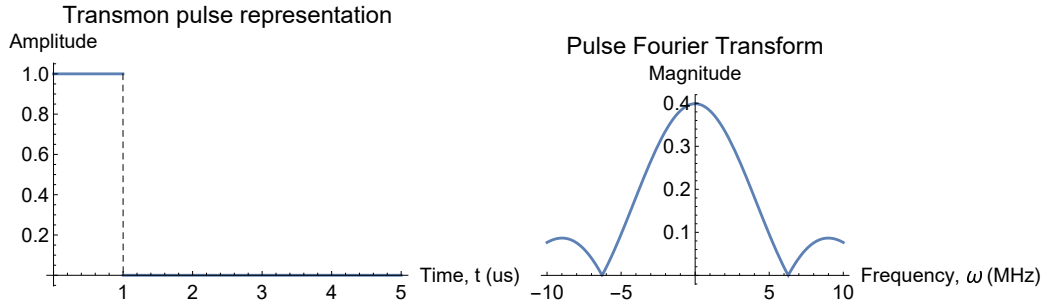

(b)

Figure A.7: a) pulse duration and corresponding Fourier transform for a long pulse b) for a short pulse.

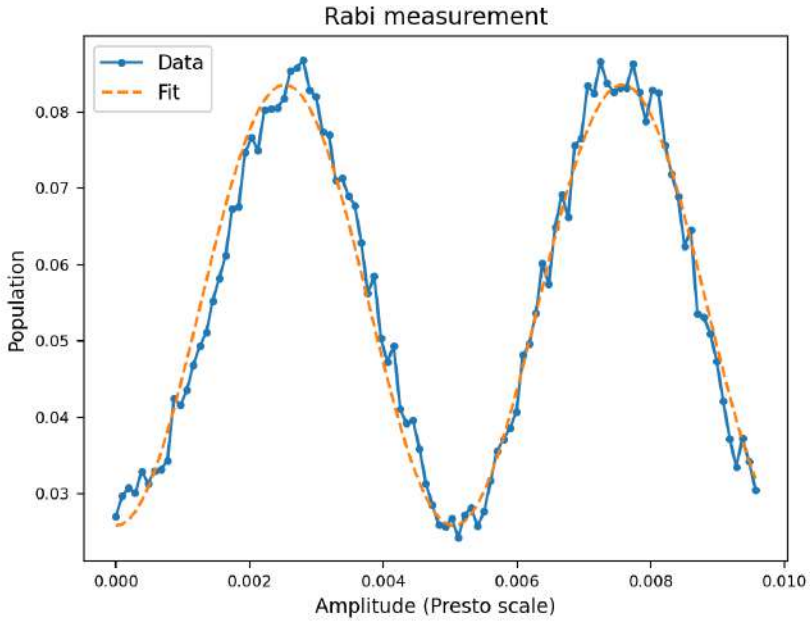

(a)

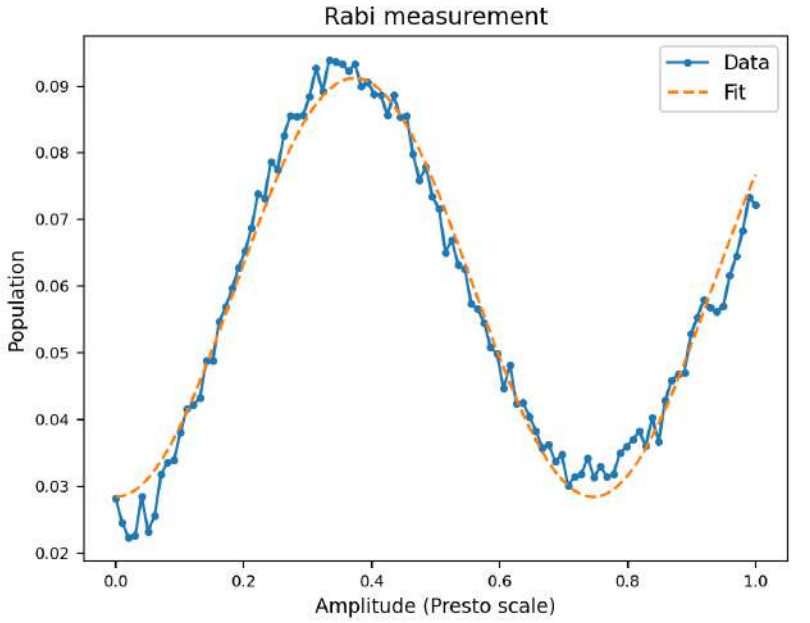

(b)

Figure A.8: a) selective and b) unselective Rabi oscillations

A.2.2.4 Qubit T_1 and T_2 measurements

Qubit's T_1 and T_2 measurements are taken in fashion similar to the one described [16]. An example of the obtained results for qubit 1 are shown in Fig. A.9.

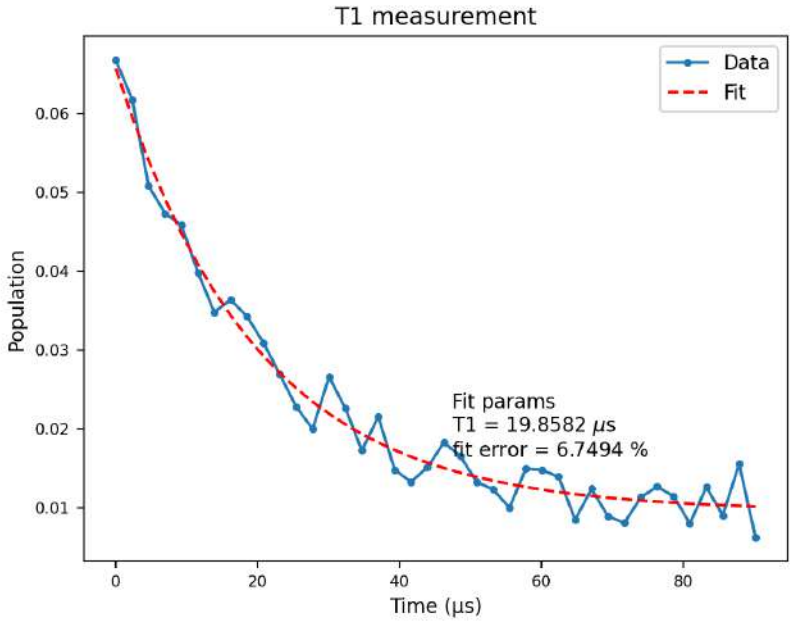

(a)

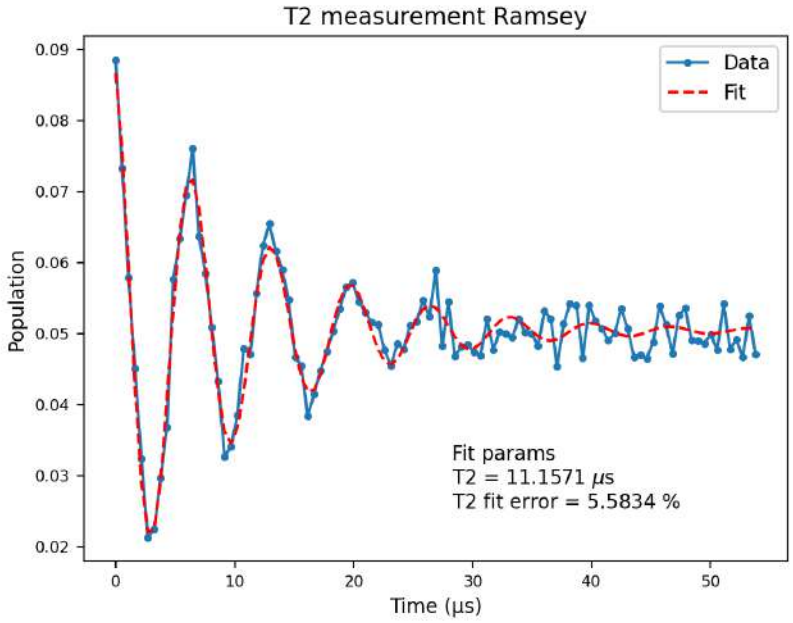

(b)

Figure A.9: Measurements of a) T_1 and b) T_2 for qubit 1

A.2.2.5 Cavity frequency measurement

To perform measurements of the cavity eigenfrequency, a continuous pulse is once again applied, with its frequency being swept. A selective π-pulse that is tailored to the cavity's state is used to populate the qubit, consequently influencing the readout

outcome. When the pulse applied to the cavity reaches resonance, the qubit ceases to be populated, resulting in the readout pulse corresponding to the resonant frequency of the readout resonator. This type of readout is termed "dispersive readout". The pulse sequence for this procedure is illustrated in Fig. A.10a, and an example of the cavity spectrum can be observed in Fig. A.10b.

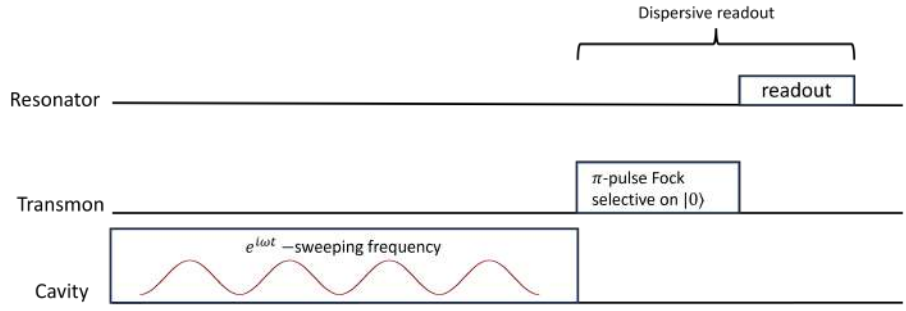

(a)

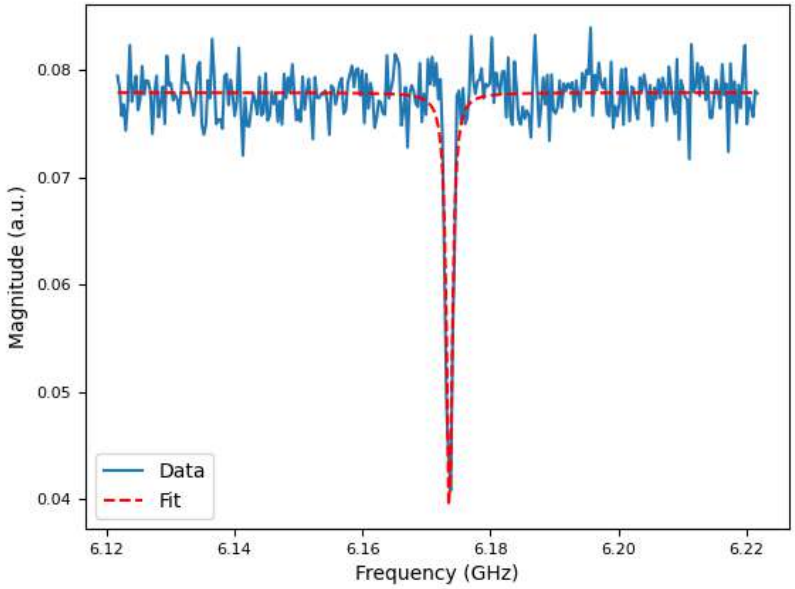

(b)

Figure A.10: a) pulse sequence for cavity spectroscopy b) Measurement of cavity 1 spectrum

A.2.2.6 Cavity Ramsey

To measure the cavity decay time T_2, the experiment involves observing Ramsey fringes. This procedure is conducted in a similar manner as described in [16], with the distinction that coherent displacement is employed instead of a $\frac{\pi}{2}$-pulse. The pulse sequence and the corresponding results are depicted in Fig. A.11.

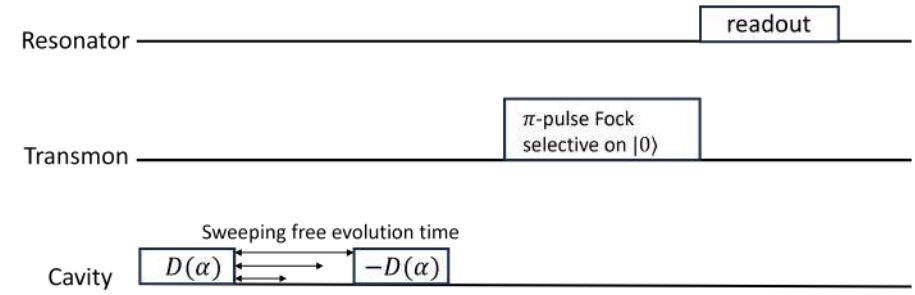

(a)

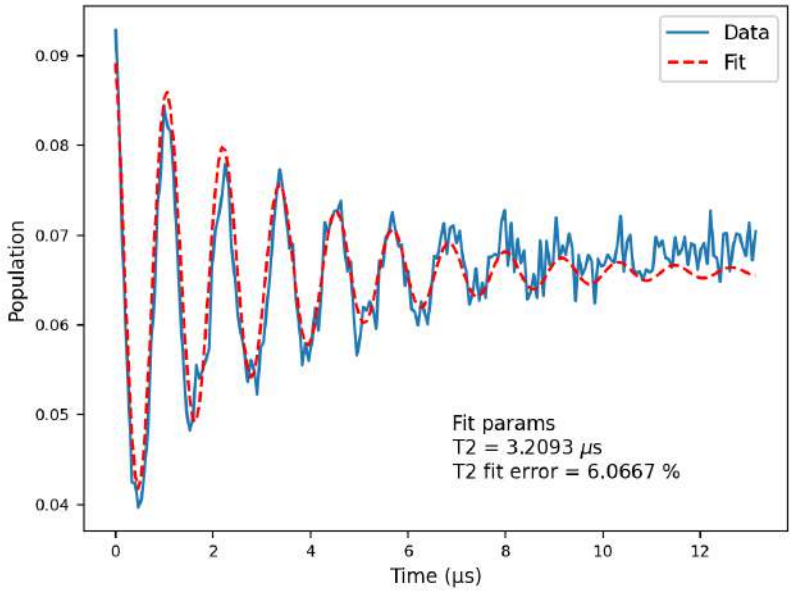

(b)

Figure A.11: a) pulse sequence for T_2 measurement b) Ramsey fringes of cavity 1.

A.2.2.7 Cavity-qubit χ

The measurement of the coupling strength χ is carried out according to the procedure illustrated in Fig. A.12a. The outcome of this experiment is presented in Fig. A.12b.

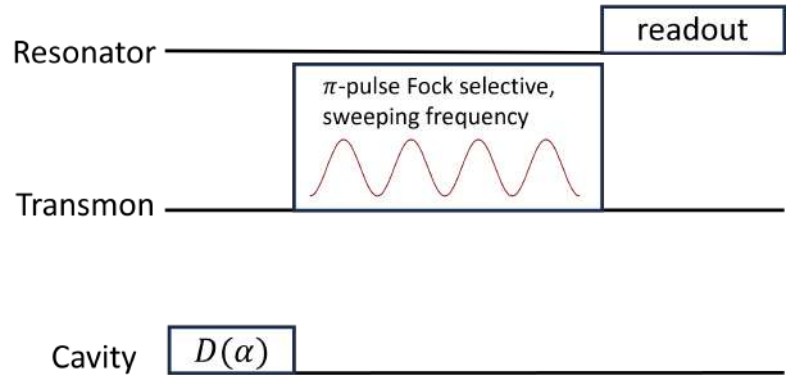

(a)

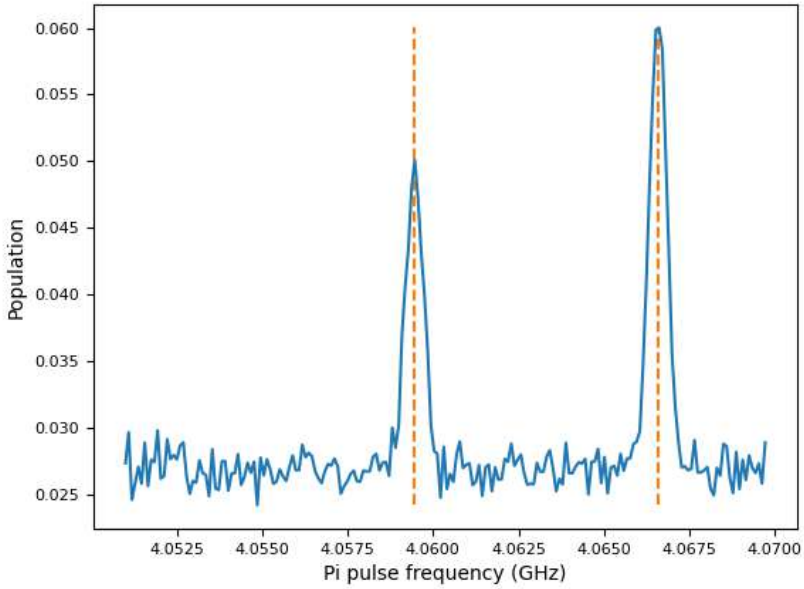

(b)

Figure A.12: a) pulse sequence for χ measurement b) Experiment result for cavity 1 and qubit 1.

A.2.2.8 Correspondence of displacement amplitude to voltage pulse amplitude

To determine the relationship between α and voltage, the pulse sequences depicted in Fig. A.13a and A.13b is employed, resulting in two distinctive population distributions. Fitting the resulting populations with Poisson distribution gives calibration scale between displacement α and applied voltage amplitude. The outcome for cavity 1 is illustrated in Fig. A.13c.

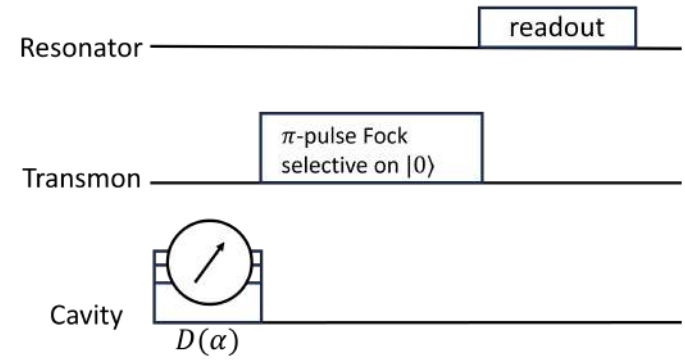

(a)

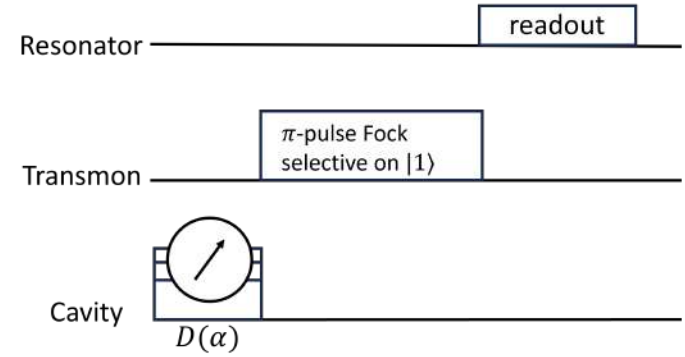

(b)

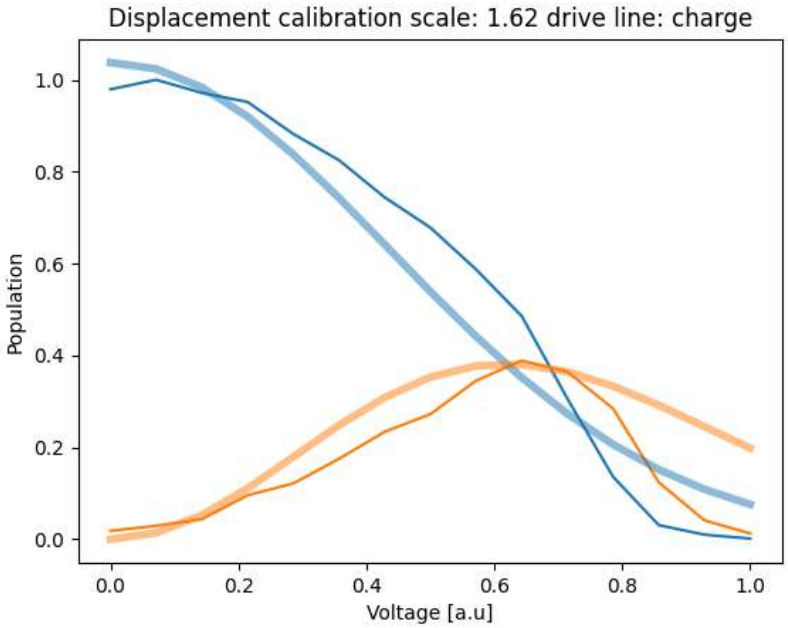

(c)

Figure A.13: a) pulse sequence, that finds the probability of $|0\rangle$ cavity state b) the probability of $|1\rangle$ cavity state c) an example of the measurement for cavity 1. The blue curve corresponds to pulse sequence in (a), and the orange curve – to pulse sequence in (b).

A.2.2.9 Cavity T_1

To find the cavity relaxation time T_1, the experiment is conducted using a methodology similar to that outlined in [16], with the modification of employing coherent displacement instead of a π-pulse. The pulse sequence and the resultant outcomes are presented in Fig. A.14.

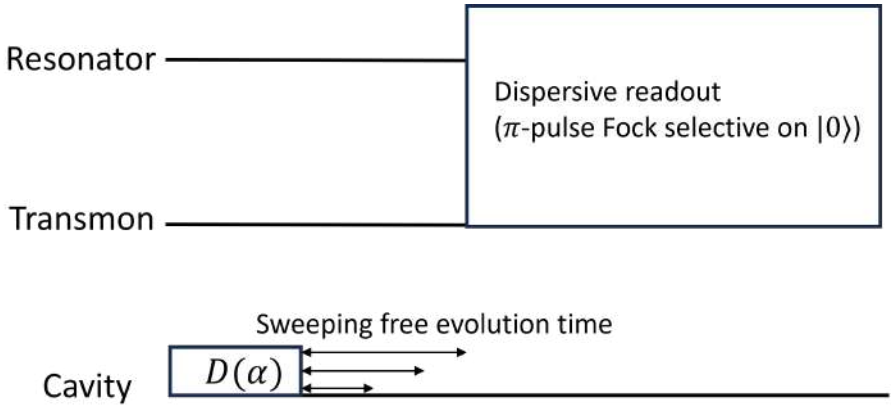

(a)

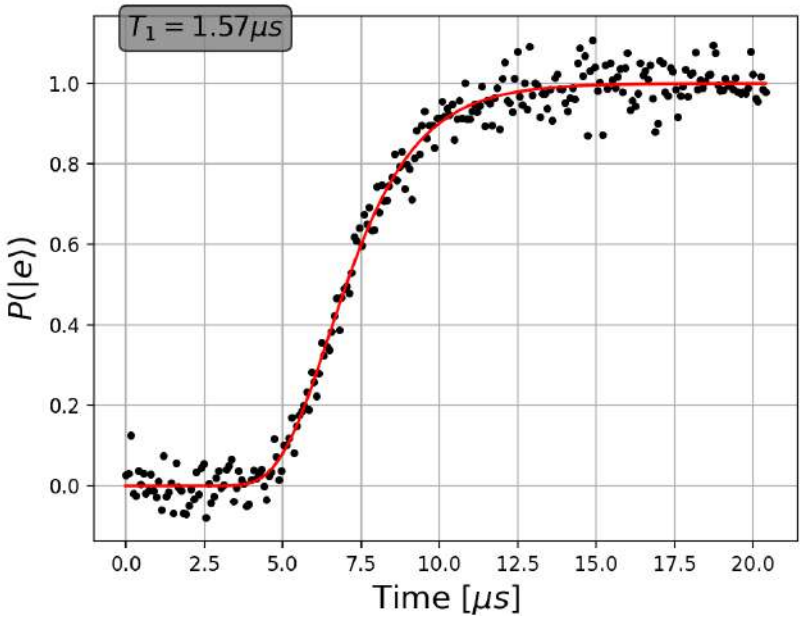

(b)

Figure A.14: a) pulse sequence for T_1 measurement. b) The experiment result for cavity 1.

A.3 Measured system parameters

A.3.1 Target vs measured parameters: frequencies

	target frequencies	measured frequencies
res 1, GHz	5.89	5.78
res 4, GHz	6.67	6.63
qb 1, GHz	4.35	4.06
qb 4, GHz	5.21	4.81
cav 1, GHz	3.72	3.71
cav 2, GHz	6.94	6.84
cav 3, GHz	3.84	-
cav 4, GHz	6.42	6.18
coupler, GHz	5.69 (sw sp)	4.605 (sw sp)

A.3.2 Target vs measured parameters: Charging energies E_C

	target E_C	measured anharmonicity α	$E_C \sim 0.9\alpha$
qb 1 , MHz	203	256.7	231
qb 4, MHz	205	205.6	185

A.3.3 Not simulated system parameters

Parameter name	Measured value
qb 1 T_1, μs	14.9
qb 4 T_1, μs	21
qb 1 T_2, μs	11.15
qb 4 T_2, μs	22.1
cav 1 T_1, μs	5.8
cav 4 T_1, μs	1.6
cav 1 T_2, μs	3.4
cav 4 T_2, μs	2.2

DEPARTMENT OF MICROTECHNOLOGY AND NANOSCIENCE
CHALMERS UNIVERSITY OF TECHNOLOGY
Gothenburg, Sweden
www.chalmers.se

CHALMERS
UNIVERSITY OF TECHNOLOGY